

Rupture process of the 2019 Ridgecrest, California M_w 6.4 Foreshock and M_w 7.1 Earthquake Constrained by Seismic and Geodetic Data

Kang Wang^{*1,2}, Douglas S. Dreger^{1,2}, Elisa Tinti^{3,4}, Roland Bürgmann^{1,2}, and Taka'aki Taira²

ABSTRACT

The 2019 Ridgecrest earthquake sequence culminated in the largest seismic event in California since the 1999 M_w 7.1 Hector Mine earthquake. Here, we combine geodetic and seismic data to study the rupture process of both the 4 July M_w 6.4 foreshock and the 6 July M_w 7.1 mainshock. The results show that the M_w 6.4 foreshock rupture started on a northwest-striking right-lateral fault, and then continued on a southwest-striking fault with mainly left-lateral slip. Although most moment release during the M_w 6.4 foreshock was along the southwest-striking fault, slip on the northwest-striking fault seems to have played a more important role in triggering the M_w 7.1 mainshock that happened ~ 34 hr later. Rupture of the M_w 7.1 mainshock was characterized by dominantly right-lateral slip on a series of overall northwest-striking fault strands, including the one that had already been activated during the nucleation of the M_w 6.4 foreshock. The maximum slip of the 2019 Ridgecrest earthquake was ~ 5 m, located at a depth range of 3–8 km near the M_w 7.1 epicenter, corresponding to a shallow slip deficit of $\sim 20\%$ – 30% . Both the foreshock and mainshock had a relatively low-rupture velocity of ~ 2 km/s, which is possibly related to the geometric complexity and immaturity of the eastern California shear zone faults. The 2019 Ridgecrest earthquake produced significant stress perturbations on nearby fault networks, especially along the Garlock fault segment immediately southwest of the 2019 Ridgecrest rupture, in which the coulomb stress increase was up to ~ 0.5 MPa. Despite the good coverage of both geodetic and seismic observations, published coseismic slip models of the 2019 Ridgecrest earthquake sequence show large variations, which highlight the uncertainty of routinely performed earthquake rupture inversions and their interpretation for underlying rupture processes.

KEY POINTS

- The 2019 Ridgecrest sequence ruptured a complex array of faults and features a shallow slip deficit.
- The low-rupture velocity is likely related to geometric complexity and immaturity of the eastern California shear zone (ECSZ).
- The earthquakes produced significant stress changes on the Garlock and other nearby faults.

[Supplemental Material](#)

INTRODUCTION

With a slip rate of ~ 40 mm/yr and total length of >1000 km, the San Andreas fault system accommodates nearly 80% of the relative motion between the Pacific and North American plates. In addition, another actively deforming fault system, including the Walker Lane and eastern California shear zone

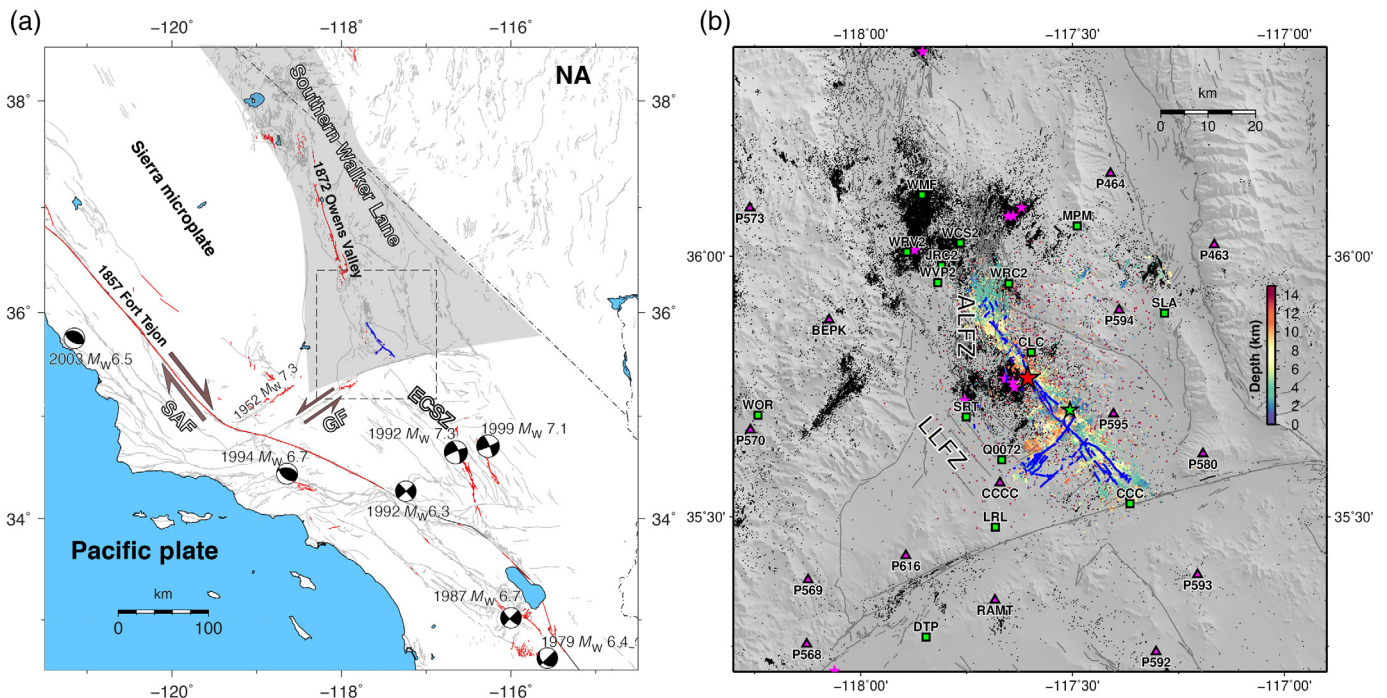
(ECSZ), roughly aligns with the California-Nevada border stretching from southern Oregon in the north to the Salton Sea in the south (e.g., [Surpless, 2008](#); [Unruh and Humphrey, 2017](#); Fig. 1). The ECSZ is a ~ 100 km wide zone of deformation, extending from the Owens Valley to the Mojave Desert near the east end of the “big bend” in the San Andreas fault (Fig. 1a). This fault system accommodates much of the remaining $\sim 20\%$ of relative motion between the Pacific and North

1. Department of Earth and Planetary Sciences, University of California, Berkeley, Berkeley, California, U.S.A.; 2. Berkeley Seismological Laboratory, University of California, Berkeley, Berkeley, California, U.S.A.; 3. Dipartimento di Scienze della Terra, Università degli Studi La Sapienza, Rome, Italy; 4. Istituto Nazionale di Geofisica e Vulcanologia, Rome, Italy

*Corresponding author: kwang@seismo.berkeley.edu

Cite this article as Wang, K., D. S. Dreger, E. Tinti, R. Bürgmann, and T. Taira (2020). Rupture process of the 2019 Ridgecrest, California M_w 6.4 Foreshock and M_w 7.1 Earthquake Constrained by Seismic and Geodetic Data, *Bull. Seismol. Soc. Am.* **XX**, 1–24, doi: [10.1785/0120200108](https://doi.org/10.1785/0120200108)

© Seismological Society of America



American plates (Carlson *et al.*, 2013). The ECSZ consists of a series of dominantly right-lateral strike-slip faults, whose individual slip rates are estimated to be generally low, ranging from 1 to 3 mm/yr from geological studies (e.g., Lee *et al.*, 2001; Amos *et al.*, 2013) to 5–8 mm/yr from geodetic observations (e.g., McClusky *et al.*, 2001; Miller *et al.*, 2001; Peltzer *et al.*, 2001; Dixon *et al.*, 2003; Liu *et al.*, 2015). Despite the generally low slip rates, the ECSZ has hosted a series of $M_w > 7$ earthquakes in the past 30 yr, including the 1992 M_w 7.2 Landers earthquake, the 1999 M_w 7.1 Hector Mine earthquake, and the 2019 Ridgecrest earthquakes occurred ~50 km to the south of the 1872 ~ M_w 7.7 Owens Valley earthquake rupture (Hough and Hutton, 2008; Haddon *et al.*, 2016), separated by the Coso geothermal area (Hauksson and Unruh, 2007).

On 4 July 2019, an M_w 6.4 earthquake struck the Indian Wells Valley near the town of Ridgecrest in southern California. This M_w 6.4 earthquake was followed by a vigorous aftershock sequence, which turned out to be foreshocks to the M_w 7.1 event, ~34 hr later. The 2019 Ridgecrest mainshock was the largest earthquake to strike the contiguous United States, since the Landers and Hector Mine earthquakes. Field surveys and satellite imagery indicate that the 2019 Ridgecrest earthquake sequence ruptured a series of nearly orthogonal conjugate faults that were not previously mapped (e.g., Ross *et al.*, 2019; Hudnut *et al.*, 2020; Milliner and Donnellan, 2020; Ponti *et al.*, 2020). According to the U.S. Geological Survey (USGS) Quaternary fault database, the closest mapped faults near the 2019 Ridgecrest earthquakes are the Airport Lake fault zone and the Little Lake fault zone (Fig. 1b), both of which are characterized by intense seismic activity before the

Figure 1. Tectonic setting of the 2019 Ridgecrest earthquake sequence. (a) Map showing the Quaternary faults and historical earthquakes in southern California. Focal mechanism plots represent centroid moment tensor solutions of $M_w > 6$ earthquakes since 1976 from Global Centroid Moment Tensor (Global CMT; Ekström *et al.*, 2012). Red curves show surface traces of historical ruptures in the past 150 yr. Blue curves are surface traces of the 2019 Ridgecrest mapped by field survey and inferred from satellite imagery. (b) A zoom-in map of relocated background seismicity from 1981 to 2018 (Hauksson *et al.*, 2012) around the 2019 Ridgecrest earthquake (black dots), and foreshocks and aftershocks ~4 days since the 2019 M_w 7.1 Ridgecrest earthquake (Shelly, 2020). Green and red stars represent epicenters of the 4 July M_w 6.4 foreshock and the 5 July M_w 7.1 mainshock, respectively. Pink triangles represent the Plate Boundary Observatory (PBO) continuous Global Navigation Satellite System (GNSS) stations. Green squares show the strong-motion sites used in this study. Pink stars are $M_w > 5$ earthquakes before the 2019 Ridgecrest earthquake sequence. ALFZ, Airport Lake fault zone; ECSZ, eastern California shear zone; GF, Garlock fault; LLFZ, Little Lake fault zone; NA, North America plate; SAF, San Andreas fault. The color version of this figure is available only in the electronic edition.

2019 Ridgecrest earthquakes, including a sequence of $M_w > 5$ events in 1995 (Hauksson *et al.*, 1995; Dreger *et al.*, 1998). However, no earthquakes larger than M_w 6 have occurred in this area in historical times.

Compared to previous major seismic events in southern California, the 2019 Ridgecrest earthquake occurred in an era of unprecedented coverage of both geodetic and seismic instrumentation. Coseismic deformation of the 2019 Ridgecrest earthquake sequence was well imaged by several Synthetic Aperture Radar and optical imagery satellite missions, including Sentinel-1, COSMO-SkyMed, Advanced Land Observation Satellite-2, Sentinel-2, and PlanetLab (e.g., Fielding *et al.*, 2020;

TABLE 1
Fault Model Geometry

	Segment	Top Center (Lat, Lon, and Depth)*	Dimension (Length and Width)	Orientation (°) (Strike and Dip)	Rake Variability (°)
M_w 6.4 foreshock	FSEG1	35.7124, -117.527, 2.9	13.65 and 13.65	312.0 and 85.0	-150 to -210
	FSEG2	35.664, -117.517, 1.2	21.45 and 13.65	224.0 and 83.0	-30 to 30
M_w 7.1 mainshock	MSEG1	35.775, -117.605, 1.0	16 and 20	331.0 and 90.0	-135 to -225
	MSEG2	35.877, -117.693, 1.0	14 and 20	320.0 and 90.0	-135 to -225
	MSEG3	35.665, -117.495, 1.0	14 and 20	307.0 and 90.0	-135 to -225
	MSEG4	35.569, -117.361, 1.0	20 and 20	314.7 and 90.0	-135 to -225
	MSEG5	35.723, -117.544, 1.0	14 and 20	311.0 and 85.0	-135 to -225

*Locations are for the center of the fault segments that are discretized into approximately $2 \times 2 \text{ km}^2$ subfaults. The shallow subfaults of FSEG2 reach 0.2 km depth, whereas surface subfaults of MSEG1–4 reach 0 km depth. Lat, latitude; lon, longitude.

Milliner and Donnellan, 2020; Wang and Bürgmann, 2020). The sequence was also well recorded by the California Integrated Seismic Network (CISN; Ross *et al.*, 2019; Hauksson *et al.*, 2020) and dozens of Global Navigation Satellite System (GNSS) stations across California and Nevada (Floyd *et al.*, 2020; Mattioli *et al.*, 2020). These data provide essential information for studying the rupture process and stress interactions between the M_w 6.4 foreshock and the M_w 7.1 mainshock, herein referred to as foreshock and mainshock.

Here, we use both geodetic and seismic data to derive the slip distributions and the rupture history of the 2019 Ridgecrest foreshock and mainshock. We then compare our models with the kinematic source models published to date to assess how model assumptions, parameterization, and used data sets affect the inferred pattern and evolution of coseismic slip. Finally, we use the obtained slip models as input to compute the static coulomb stress transfer between the M_w 6.4 foreshock and the M_w 7.1 mainshock, as well as the stress change on nearby fault networks.

DATA AND METHODS

Data

Geodetic data used in this study include Sentinel-1 Interferometric Synthetic Aperture Radar (InSAR), and static and 5 Hz high-rate GNSS (hr-GNSS) observations from continuously operating stations maintained by the UNAVCO. Detailed information about the Sentinel-1 InSAR processing and resulting data products are described in Wang and Bürgmann (2020). All available Sentinel-1 interferograms span both the M_w 6.4 and 7.1 events. Static coseismic GNSS displacements due to both the M_w 6.4 foreshock and the M_w 7.1 mainshock are from the Scripps Orbit and Permanent Array Center (SOPAC). The hr-GNSS solutions are also from SOPAC (Peng Fang, written communication, 2019).

Seismic waveform data from CISN were obtained from the Southern California Earthquake Data Center (2013). The data were corrected for instrument response and integrated to velocity for the foreshock and to displacement for the

mainshock. For the M_w 7.1 mainshock, no low-pass filter was applied; however, for most stations a causal (one pass and four poles) 0.01 Hz high-pass filter was applied to remove long-period noise. The exceptions to this were for stations CLC, LRL, and SRT, in which significant static offsets (~ 12 cm at LRL, ~ 30 cm at SRT, and ~ 100 cm at CLC) were observed, and for the hr-GNSS time series from stations CCCC (~ 20 cm) and P595 (~ 50 cm). In contrast, the foreshock data (both strong motion and hr-GNSS) were filtered in velocity between 0.02 and 0.4 Hz with high-pass and low-pass filters (two passes and four poles). The latter is needed to remove the site effects that are significant in this area.

Inversion method

Joint inversion using both seismic and geodetic data.

Here, we describe the general kinematic inversion method, and specific choices of key parameterizations are provided in the following Results section. The kinematic method that we use to simultaneously invert seismic waveforms, GNSS static offsets, hr-GNSS, and InSAR deformation data is based on the multiple time-window approach of Hartzell and Heaton (1983), as implemented by Kaverina *et al.* (2002). This approach allows for variable slip direction, as well as temporal heterogeneity of the rupture velocity and rise time in a linear, non-negative least squares inversion. Models are constructed using multiple planar fault segments (see Fig. S1, available in the supplemental material to this article, for a graphic illustration of this method).

The kinematic model describes the spatiotemporal distribution of moment or slip, the rupture speed, and the slip rise time. Multiple “time windows” are used to allow for heterogeneity in the rupture velocity and rise time, as well as to solve for the slip vector (e.g., Hartzell and Heaton, 1983). The slip vector is found from the linear sum of slip inferred at different time windows on each subfault, accounting for variable rake angles (see Tables 1 and 2). Isosceles triangles or boxcars are assumed for the slip velocity function (i.e., source time function). A minimum rise time is chosen such that its duration is

TABLE 2
Rupture Kinematics of the 2019 Ridgecrest Earthquake Sequence

	Segment	Rupture Velocity (km/s)	Peak and Average Slip (m)*	Mean and S.D. and Rake (°)*	Average Rise Time (s)*	Moment (N·m)
Foreshock inversion results: $M_0 5.12 \times 10^{18}$ N·m (M_w 6.44)	FSEG1	2.5	1.28 and 0.3	-192.0 and 12.6	3.0	1.83×10^{18}
	FSEG2	1.9	1.84 and 0.65	+1.3 and 17.4	3.4	3.28×10^{18}
Mainshock inversion results: $M_0 4.69 \times 10^{19}$ N·m (M_w 7.05)	MSEG1	2.2	4.69 and 2.99	-178.8 and 9.7	5.3	1.79×10^{19}
	MSEG2	2.2	5.59 and 1.97	-183.9 and 29.5	5.4	8.52×10^{18}
	MSEG3	2.2	4.21 and 1.84	-188.7 and 13.1	5.6	5.82×10^{18}
	MSEG4	2.2	4.61 and 1.98	-194.6 and 15.7	4.0	4.77×10^{18}
	MSEG5	2.2	4.01 and 1.84	-164.9 and 22.5	5.2	9.92×10^{18}

*Slip, rise time, and rake averages are computed for sub faults having slip >20 cm. S.D., standard deviation.

consistent with the time of rupture propagation across a unit subfault. Each time-fault segment uses this minimum rise time, but the time-fault segments overlap to allow for the possibility that a given subfault can rupture multiple times, thereby allowing for variable rise time. The time-fault segments overlap by one half of the minimum rise time. The overall rise time for each subfault is then the sum of the same subfault staggered over the overlapping time windows. See Figure S1 for a schematic of the model construction.

For faults with changing strike or dip over the rupture, multiple fault segments are employed. The timing of the segments is specified for a starting subfault on each segment, which is defined by the delay time for rupture across previous segments, or can be optimized using a grid search for optimal timing (e.g. Dreger *et al.*, 2004; Benetatos, *et al.*, 2007). Table 1 lists the key model parameters of the kinematic rupture modeling for the foreshock and mainshock.

As these finite-source kinematic models are typically under-determined, further regularization in the form of a slip positivity constraint (the fault cannot slip backward) and spatial smoothing are applied. As described in Kaverina *et al.* (2002), the weight of the spatial smoothing constraint is found through trade-off analysis in which the smoothest model that retains nearly the maximum fit to the data is chosen. We also evaluate the weighting of the three datasets used in the inversion to find a value that provides balanced maximum fit to each dataset (e.g., Kaverina *et al.*, 2002; Dreger *et al.*, 2015). We quantify the model performance by computing the data variance reduction (VR) to each data type, which is defined as

$$VR = 100\% \times \left(1 - \frac{\sum (d - d')^2}{\sum d^2} \right),$$

in which d and d' represent the vectors of observations and model predictions, respectively.

Because the two earthquakes occurred close in time, the ascending and descending Sentinel-1 interferograms include

contributions from both earthquakes. Therefore, we used an iterative approach in the modeling to isolate the contributions of the two earthquakes. The procedure has the following steps:

1. Seismic waveforms, the hr-GNSS time series, and the static GNSS displacements were inverted for the M_w 6.4 earthquake. The resulting model was then used to estimate the InSAR line of sight (LoS) displacements due to the foreshock.
2. The predicted foreshock LoS displacements were then removed from the interferograms for use in the simultaneous inversion with seismic waveforms, hr-GNSS time series, and static GNSS displacements for the mainshock.
3. The predicted InSAR LoS displacements for the mainshock were removed from the original InSAR data to estimate a new mainshock InSAR residual displacements field.
4. The mainshock InSAR residual displacements within an elliptical area around the M_w 6.4 rupture (see Fig. S2 for the spatial extent of the ellipse) were then used in a joint inversion of seismic waveforms, hr-GNSS time series, and static GNSS displacements for the foreshock.
5. Finally, the foreshock InSAR residual displacements were used in a joint seismic, GNSS, and InSAR inversion for the mainshock rupture process.

Through this process, the contributions from the foreshock and mainshock to the InSAR LoS deformation data were effectively isolated for the two events.

Kinematic model detail for the foreshock. The fault model for the foreshock consists of a northwest-striking plane (FSEG1) and a southwest-striking plane (FSEG2) that is nearly orthogonal to the mainshock rupture plane (Fig. 2). Table 1 lists the location of the fault segments, their dimension, orientation, and the range of slip directions allowed in the inversion.

The assumed fault geometry is refined during the initial inversions by slightly varying the strike and dip parameters of both fault planes, starting from the Global Centroid Moment

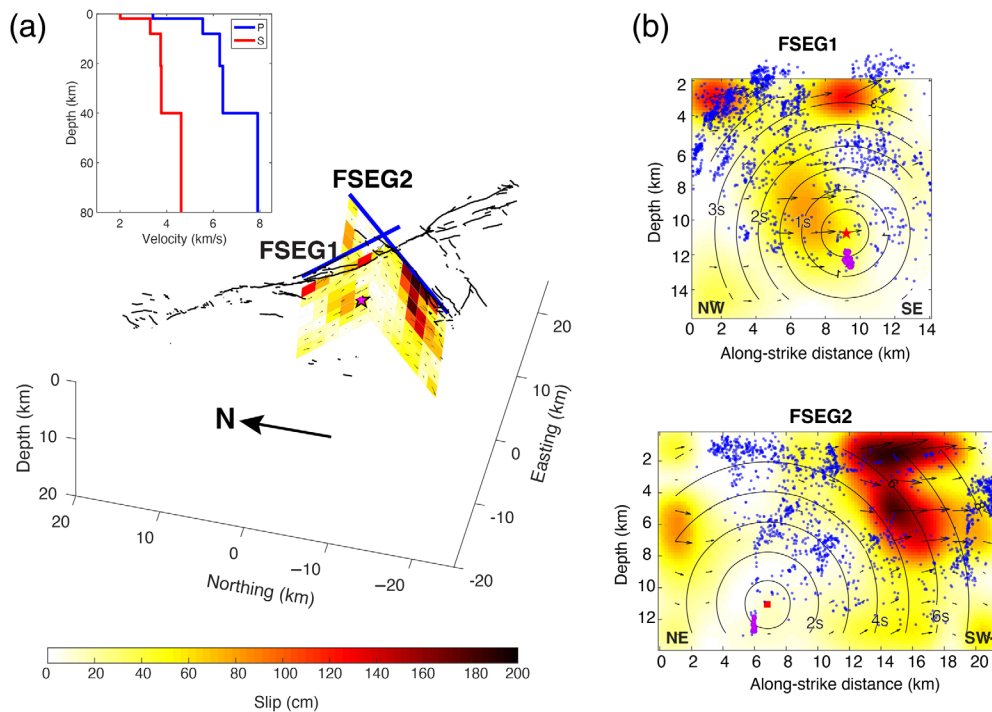


Figure 2. Coseismic slip model of the M_w 6.4 foreshock of 2019 Ridgecrest earthquake sequence. (a) Slip distribution in a 3D perspective. Inset shows the seismic velocity structure for computing Green's functions in this study. Black lines represent the surface traces of the 2019 Ridgecrest rupture verified by the U.S. Geological Survey (USGS) field survey (Ponti *et al.*, 2020). (b) Slip distribution on the two fault segments. Dots are relocated aftershocks (Shelly, 2020) within 1 km of the model fault surfaces that occurred before the M_w 7.1 mainshock. Magenta circles represent foreshocks before the M_w 6.4 event (Shelly, 2020), and red star indicates the M_w 6.4 hypocenter. Red square represents the starting rupture location of the second fault FSEG2. The color version of this figure is available only in the electronic edition.

Tensor solution, to fit the distribution of the seismicity that occurred before the M_w 7.1 event (Shelly, 2020). The seismicity suggests that the northwest-striking FSEG1 has a slight deviation from vertical toward the northeast, and the southwest-striking FSEG2 dips steeply to the northwest. There is no geodetic evidence that the foreshock rupture along the northwest-striking segment FSEG1 produced significant (>20 cm) surface offset (Milliner and Donnellan, 2020). Therefore, we modeled the FSEG1 fault plane as a buried fault with the center of the shallowest subfaults located at 3 km depth. The rupture history depends on the timing and location of the assumed foreshock hypocenter, which defines the absolute location of the first fault plane. The CISN solution 35.7052° N, -117.506° W, and 10.71 km depth was adopted.

The inversion was performed by varying, through trial and error, the rise time of each time window (from 1 to 2 s with steps of 0.1 s), the rupture velocity of both the adopted fault planes (from 1.6 to 3 km/s with steps of 0.1 km/s), and the time delay of rupture initiation on the second fault segment. The rake is allowed to vary $\pm 30^\circ$ from pure right-lateral strike slip on the northwest-striking fault and pure left-lateral faulting on the southwest-striking fault. The starting rupture

location on the second fault is assumed a priori as the sub-fault closest to the hypocenter location.

Kinematic model detail for the mainshock. The mainshock rupture consists of four segments along the main fault (MSEG1–4), and a spur fault that extends southeast of the epicenter approximately 1–3 km from the main fault (MSEG5). The northeast spur fault segment MSEG5 is at the same location as the foreshock segment FSEG1. Table 1 lists the specifics concerning the location of the fault segments, their dimension, orientation, and the degree of freedom of the slip direction allowed in the inversion. Positions of subfaults are defined by their center. The CISN epicenter of 35.775° N– 117.605° W was used, with an assumed focal depth of 9 km to ensure that the top row of 2×2 km² subfaults did not extend above the free surface.

We tested different hypocentral depths, including one as shallow as 4 km as suggested by precise event relocations (Lin, 2020; Lomax, 2020). We found that the results did not strongly depend on the assumed hypocentral depth.

The minimum rise time is assumed taking into account the observation from Heaton (1990) that on average the rise time is approximately 10% of the rupture duration, or the rise time scaling relationship of Somerville *et al.* (1999), as well as using a minimum rise time that is not less than the rupture time across a unit subfault. For the mainshock, we settled on a minimum rise time of 1.0 s. We then allow for rise time variability using 12 time windows that overlap in time by 0.5 s (half of the minimum rise time), giving a possible rise time range from 1.0 to 6.5 s. Although the rupture velocity is constant for each inversion, the multiple time-window parameterization does allow for some variation in rupture velocity, depending on when the slip occurs (in the first or in a later time window) for each of the subfaults. We assume that the dip of the mainshock plane (MSEG1–4) is vertical; however, foreshock and aftershock locations (Shelly, 2020) suggest that there may be a slight dip of the northeast spur, and we used a dip of 85° to the northeast (MSEG5).

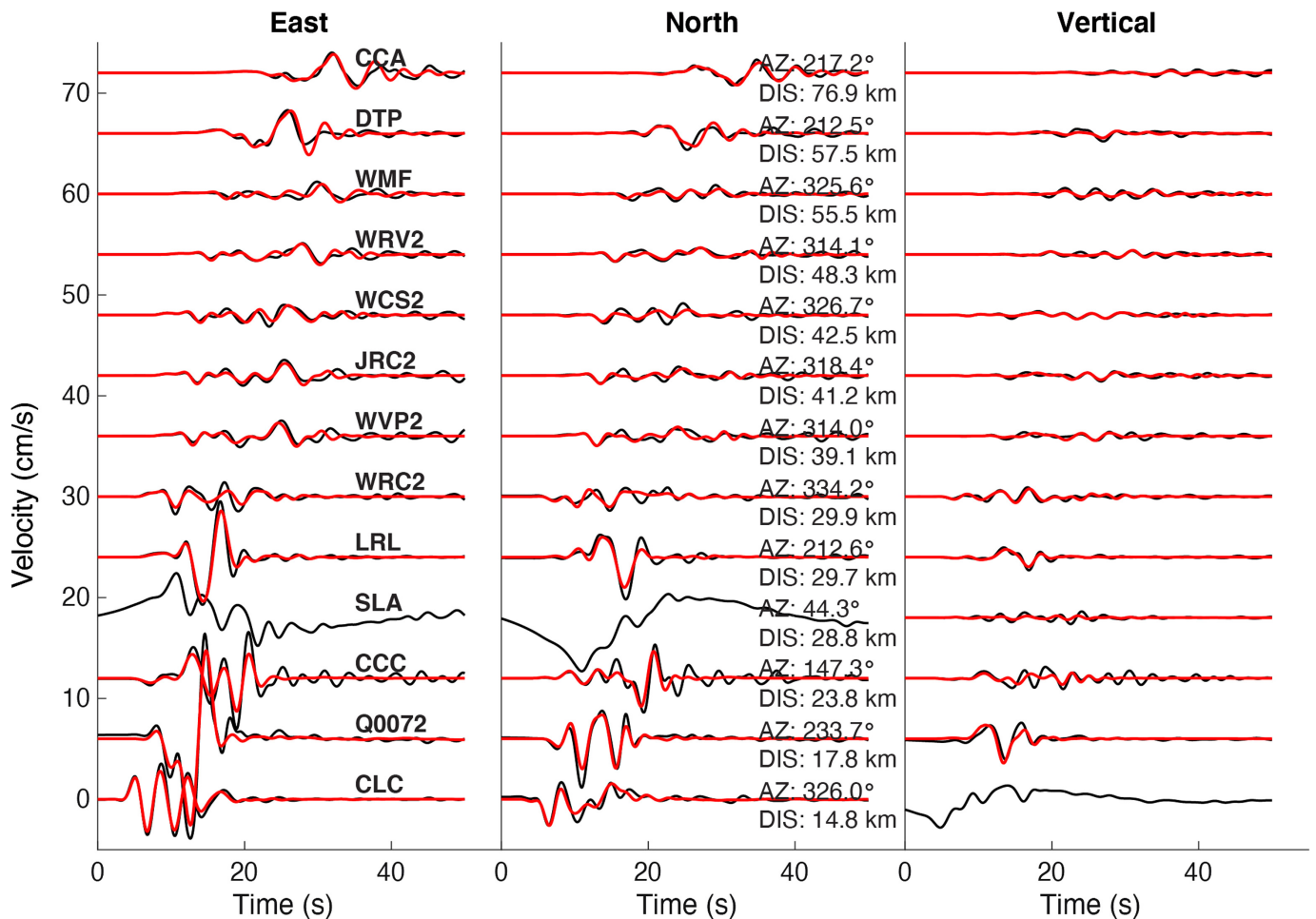


Figure 3. Observed (black) and modeled (red) strong-motion waveforms in velocity (cm/s) for the M_w 6.4 foreshock. Three time series (horizontal components of SLA station and the vertical component of CLC) are not inverted because of the low-frequency noise affecting the signal. The color version of this figure is available only in the electronic edition.

Green's functions

We used a layered velocity model estimated from observed surface wave delays by Robert Herrmann (Western United States, written communication, 2019). The model has four crustal layers above the Moho, which is located at a depth of 40 km (see Fig. 2a, inset). For the local and near-regional stations less than 150 km from the earthquakes, the Moho discontinuity does not significantly contribute to the seismic waveforms. The model has a thin (1.9 km) shallow layer with a relatively slow shear-wave velocity of 2.0 km/s. The time-series Green's functions were computed using the Herrmann (2013) frequency-wavenumber integration program hspec96. Static displacement Green's functions were computed using the EDGRN/EDCMP software of Wang *et al.* (2003).

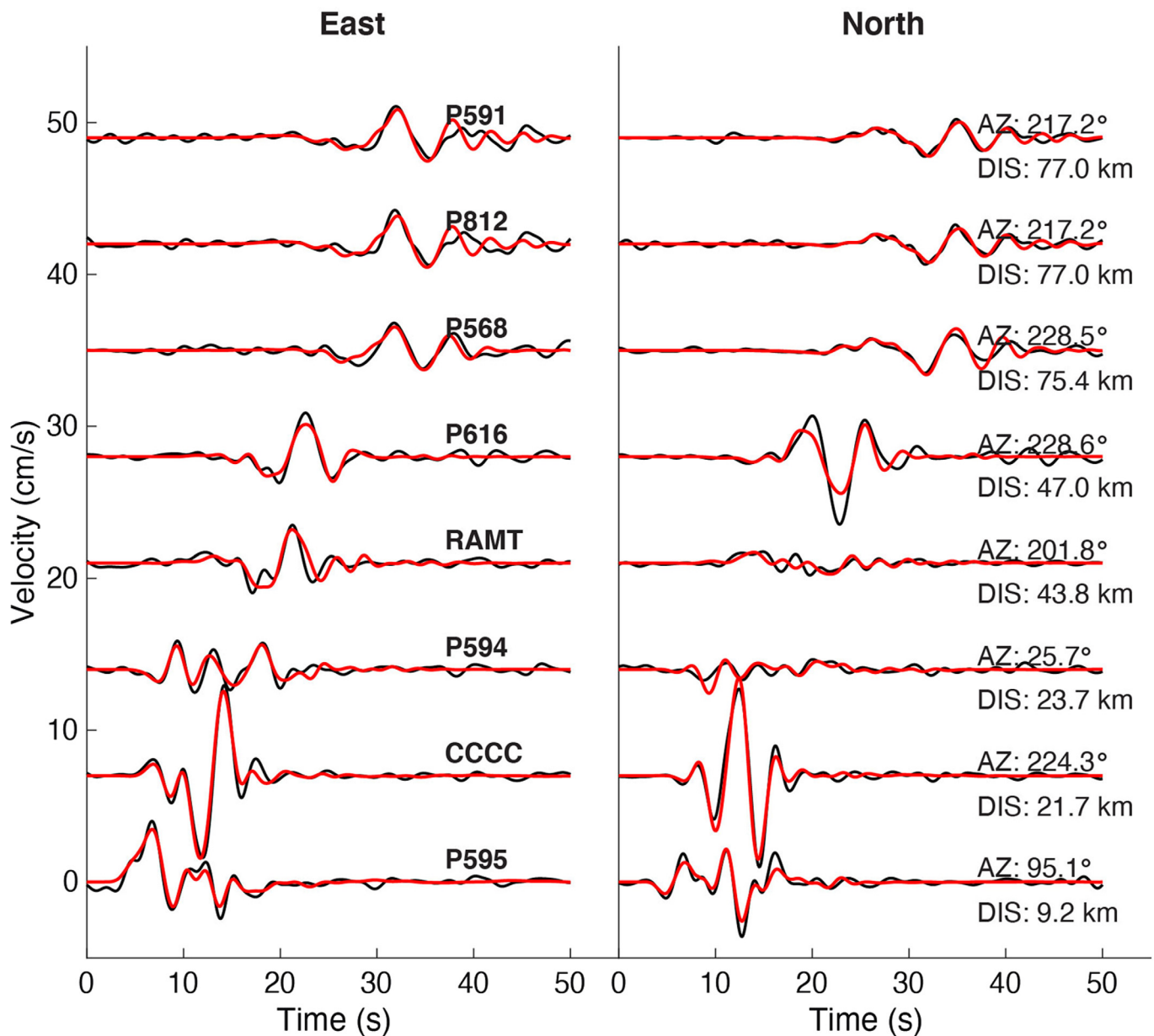
RESULTS

The M_w 6.4 foreshock

We compute a preliminary kinematic source model of the M_w 6.4 event by inverting the strong-motion data, static GNSS, and hr-GNSS data (see Fig. 1b for station locations used during the inversion), which can be considered to be solely due to the coseismic phase of the M_w 6.4 event. Because of the rupture-process complexity of this event, we first run a large number

of inversions of this dataset to determine the geometry and dimension of the involved fault planes (i.e. strike, dip, length, width, and geometric center locations of the respective fault segments). The preferred fault model is chosen as the one that yields the highest VR in predicting the surface deformation data. We then solve for the kinematic parameters, including slip distribution (amplitude and rake), rise time and rupture velocity of each time window, and the delay time of rupture initiation on the second fault that best characterize the event. The final inversion is run by also incorporating the InSAR dataset corrected for contributions from the mainshock, as described previously. We find that the two conjugate rupture segments (one striking northwestward and the other striking southwestward) are required to satisfactorily fit all the datasets.

During the initial trials, the procedure obtained negative delay times on the northwest-striking fault FSEG1, which



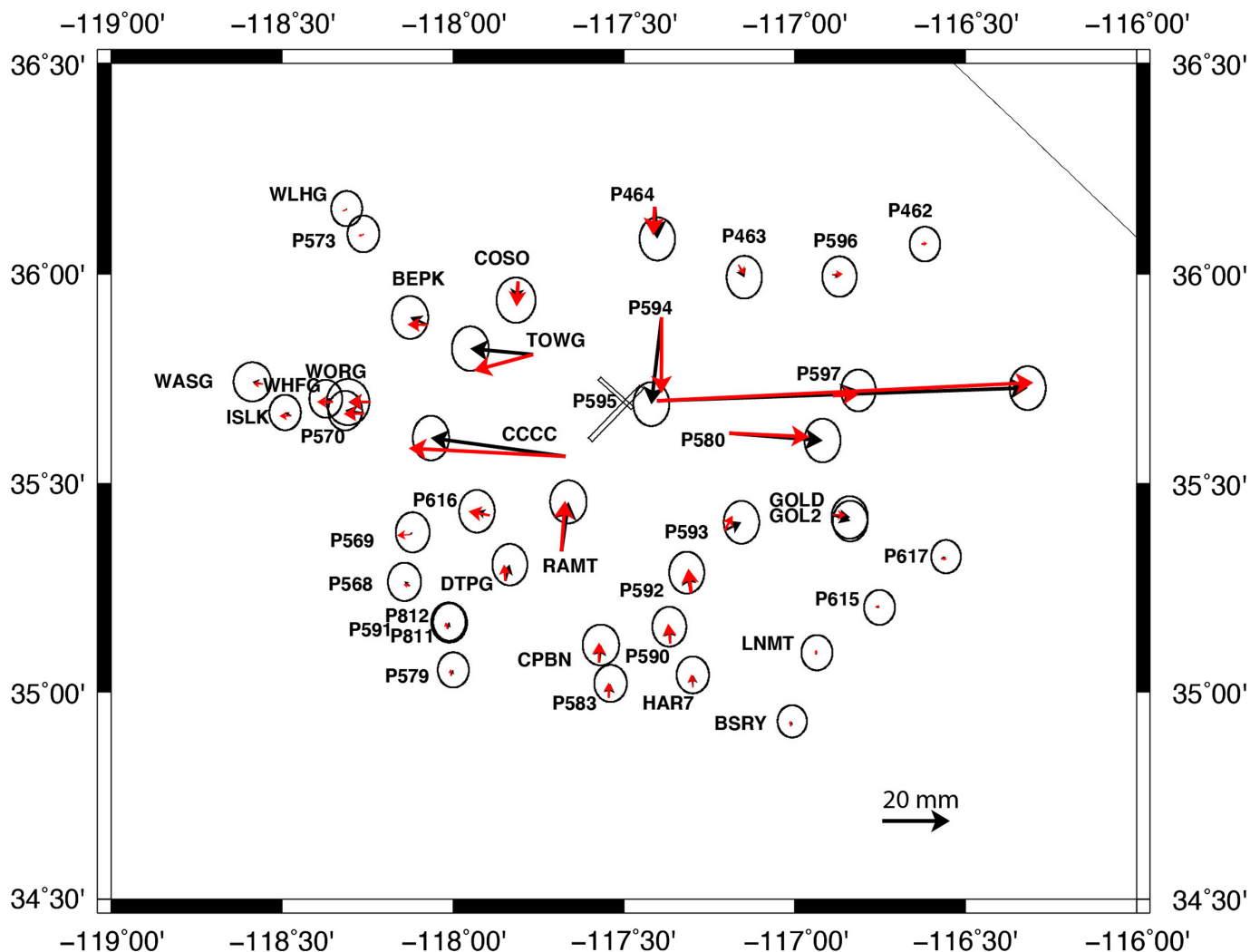
was originally considered to be a secondary rupture segment. Therefore, we decided to solve for the delay time for the FSEG2 (southwest-striking) fault, assuming that the rupture initiated on the northwest-striking fault. Considering FSEG1 to be the initial rupture segment allowed us to find an ensemble of models with a higher value of VR. Initiation of the M_w 6.4 rupture on the northwest-striking segment is consistent with independent evidence, including the observation of its immediate foreshocks and early aftershocks being aligned in that direction, indicating early slip on a deep northwest-striking structure that has little or no intersections with the southwest-striking fault segment (Huang *et al.*, 2019; Lomax, 2020; Shelly, 2020).

We find that five overlapping time windows are required to have a satisfactory fit of the data. The preferred model

Figure 4. Comparison of high-rate (hr)-GPS velocity time series due to the M_w 6.4 foreshock between observations (black) and model predictions (red). The color version of this figure is available only in the electronic edition.

produces a VR to the seismic waveforms and hr-GNSS data exceeding 80%, and more than 98% for the static GNSS data. The model also fits the InSAR data well with a VR exceeding 80%, even though we assigned the InSAR data a lower weight compared to the other datasets (the low weight is due to potential contamination by deformation from the M_w 7.1 event remaining in the InSAR data). Table 2 gives the kinematic parameters for each fault segment of the final preferred model.

The main contribution to the deformation during the M_w 6.4 event comes from the southwest-striking fault, whose



overall ~20 km long rupture propagated almost unilaterally toward the southwest from the hypocenter (Fig. 2; Table 2). A more modest contribution of seismic moment comes from the northwest-striking fault strand (FSEG1), on which the rupture started. The rupture velocities on the southwest-striking fault strand (FSEG2) and the northwest-striking strand (FSEG1) are 1.9 and 2.5 km/s, respectively (Table 2). The rise time of each individual time window is 1.3 s. Because we adopt five time windows staggered by half the rise time, the total rise time for each subfault ranges from 1.3 to 3.9 s (Table 2).

The seismic energy is initially radiated from a small patch of slip around the hypocenter on the northwest-striking fault plane (FSEG1), and no slip is found at that time close to the hypocenter on the southwest-striking fault plane (FSEG2). About 4 s after the origin time, a significant contribution of seismic energy comes from the main patch of the southwest-striking fault FSEG2 located more than 5 km away from the hypocenter. The maximum slip reaches almost 2 m and is located just below the observed peak slip zone of the surface rupture along the southwest-striking fault strand. The preferred model exhibits around 1 m of slip on two shallow

Figure 5. Comparison of horizontal GPS displacements between observations (black) and model predictions (red) due to the M_w 6.4 foreshock. Black rectangles denote the surface projections of the two conjugate fault planes used in the model. The color version of this figure is available only in the electronic edition.

patches of the buried FSEG1 fault plane, which could be an artifact of the limited data resolution.

The low-rupture velocity found along the southwest-striking fault strand is consistent with subshear (below shear-wave velocity) rupture propagation even at shallow depth, in which the S -wave velocity of the adopted velocity structure is 2.0 km/s. Because of the large number of inverted parameters, we cannot confidently resolve the trade-off between the delay time of the initial rupture on the southwest-striking fault FSEG2 and the rupture velocity. However, it appears that the main asperity of the southwest-striking fault starts to radiate energy by about 4 s after the origin time.

The preferred model fits both the surface displacement and strong-motion observations well. Figures 3 and 4 show the

comparison between the observed (black) and predicted (red) time series in velocity (cm/s) for the three-component strong-motion data and the horizontal hr-GNSS components, respectively. Figure 5 shows the comparison between the observed and predicted horizontal displacements at 41 GNSS stations. The fitting to the InSAR data is shown in Figure S2.

The M_w 7.1 mainshock

For the M_w 7.1 mainshock, we allow for variable slip direction. Table 2 gives the average rake and the standard deviation for each of the fault segments. The resulting slip model of the M_w 7.1 mainshock is shown in Figure 6. In contrast to the M_w 6.4 foreshock, coseismic slip of the M_w 7.1 event is predominantly right-lateral strike slip; however, there are local regions within the model in which minor dip slip is observed. Most notably, this occurs at an along-strike distance of 5–10 km northwest of the epicenter in which the eastside of the fault is up relative to the westside of the fault. It is in this region where surface observations indicate a graben feature with the westside of the fault moving down. The graben feature is evident in the ascending scene InSAR residuals in which there is a localized region of increased LoS on the westside of the fault during both the coseismic and early postseismic phases (Wang and Bürgmann, 2020). We attempted to model this feature; however, the parameterization of the model is too coarse in that the fault structure would be one or two 2 km long subfaults. Because the data are already being fit at a high level, and this feature does not significantly affect the seismic radiation, we elected not to incorporate this small-scale model feature to fit only the InSAR data.

Figure 7 shows that the rupture propagated bilaterally, and the kinematics (see animation in supplemental material) indicates that ruptures on the northwest segment (MSEG1) north and south of the hypocenter, and the northeast spur (MSEG5) occurred nearly simultaneously during the first a few seconds. Slip on MSEG3 was initially relatively weak, and in later time windows the slip on this segment grew to the maximum observed slip (Fig. 6). Interestingly, the junction between the southwest-striking M_w 6.4 plane and the mainshock plane seems to mark a significant contrast between the high slip of the initial rupture to the north and lower levels of slip to the south of the juncture. In addition, the initial rupture front does appear to delay slightly, as it progresses southward, and then subsequently achieves its prior rupture speed. There are three main slip asperities in the model: one located northwest of the hypocenter, one immediately southeast extending to the junction between the M_w 6.4 and mainshock faults, and the third approximately 20–30 km southeast of the hypocenter, which radiates 12–18 s after the initiation of rupture (Figs. 6 and 7).

The maximum rupture velocity in the model, which defines the timing of the first time window, is 2.2 km/s, which is about 67% of the shear-wave velocity between 1.9 and 8 km depth in which most of the slip is located. The multiple time-window approach allows slip to occur later, which can be interpreted as a deviation in rupture speed. The maximum rupture velocity is found through trial-and-error modeling. An animation of the kinematic rupture in the supplemental material shows that locally the rupture velocity is slightly slower than the prescribed value, and that the rise time across the rupture tends to be relatively long (Table 2).

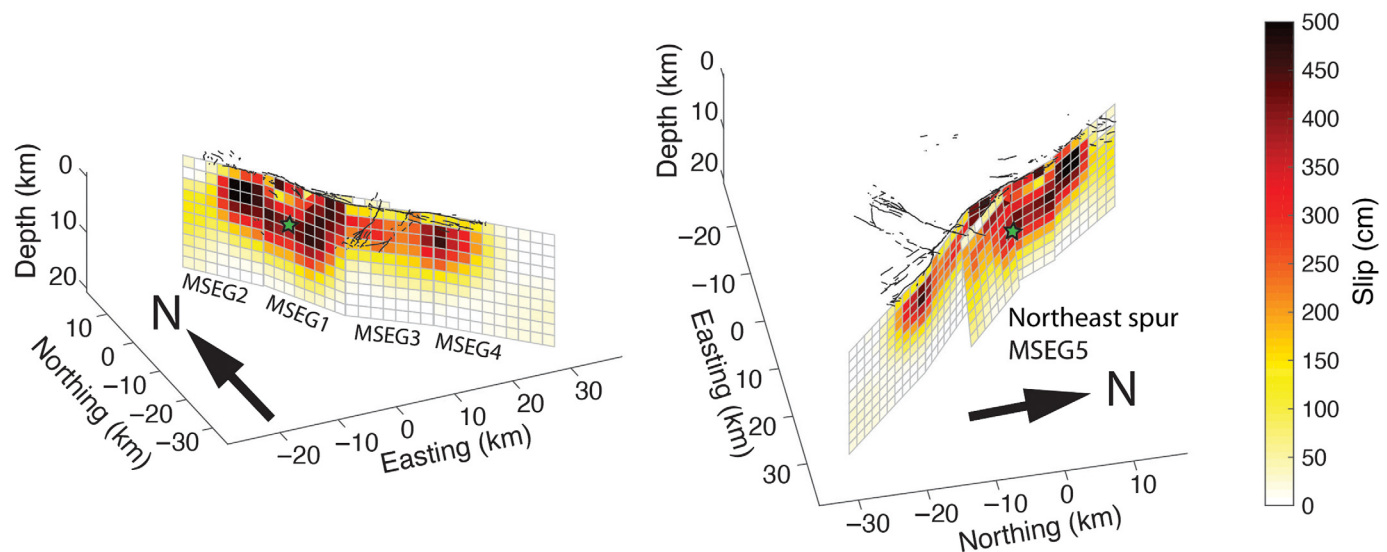


Figure 6. 3D perspectives of the mainshock kinematic model. The green star shows the hypocenter location and the juncture of the mainshock planes

and the northeast Spur fault. The color version of this figure is available only in the electronic edition.

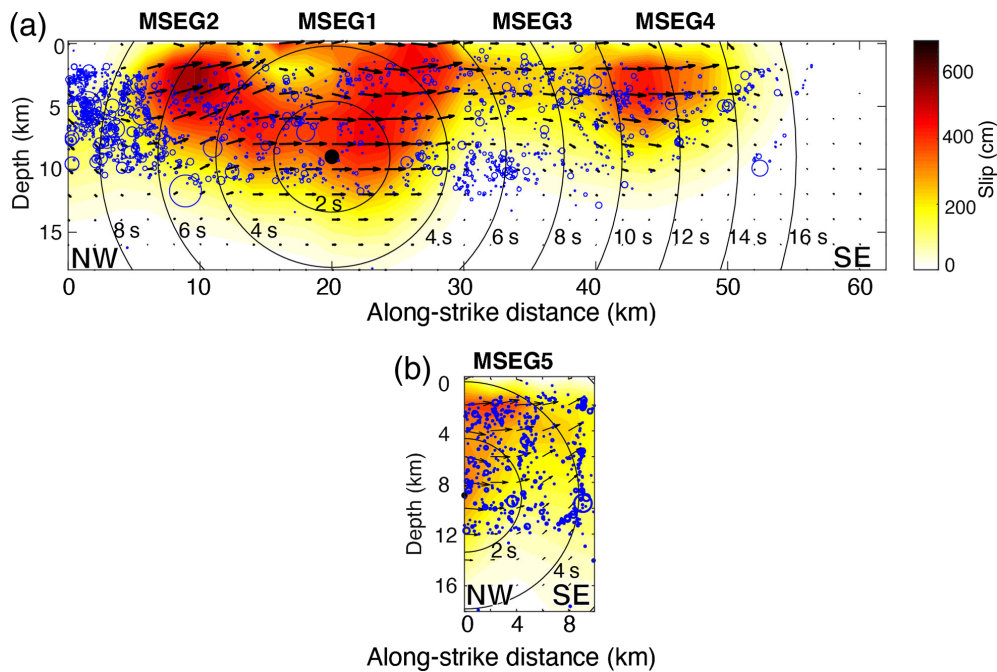


Figure 7. Fault-normal view of the mainshock slip model with the slip vectors showing the motion of the eastside of the fault model. (a) For segments MSEG1-4, and (b) for northeast spur (MSEG5). Black circle shows the hypocenter position. Circular rupture fronts for a rupture velocity of 2.2 km/s are plotted. Blue circles show relocated aftershocks of the M_w 7.1 event (from Shelly, 2020). The color version of this figure is available only in the electronic edition.

The preferred model is able to fit all of the datasets at a very high level of VR (e.g., seismic waveform 94.9%, static GNSS 97.3%, and InSAR 97.0%). Figures 8 and 9 show the comparisons of observed, and model predicted three-component displacement seismograms and InSAR LoS displacements, respectively. The fitting to the static GNSS data is shown in Figure S3. Although surface slip observations were not included in the inversion, a forward comparison with the optical-imagery-derived results of Milliner and Donnellan (2020) shows the predicted surface offsets from the model agree well with those observations (Fig. S6).

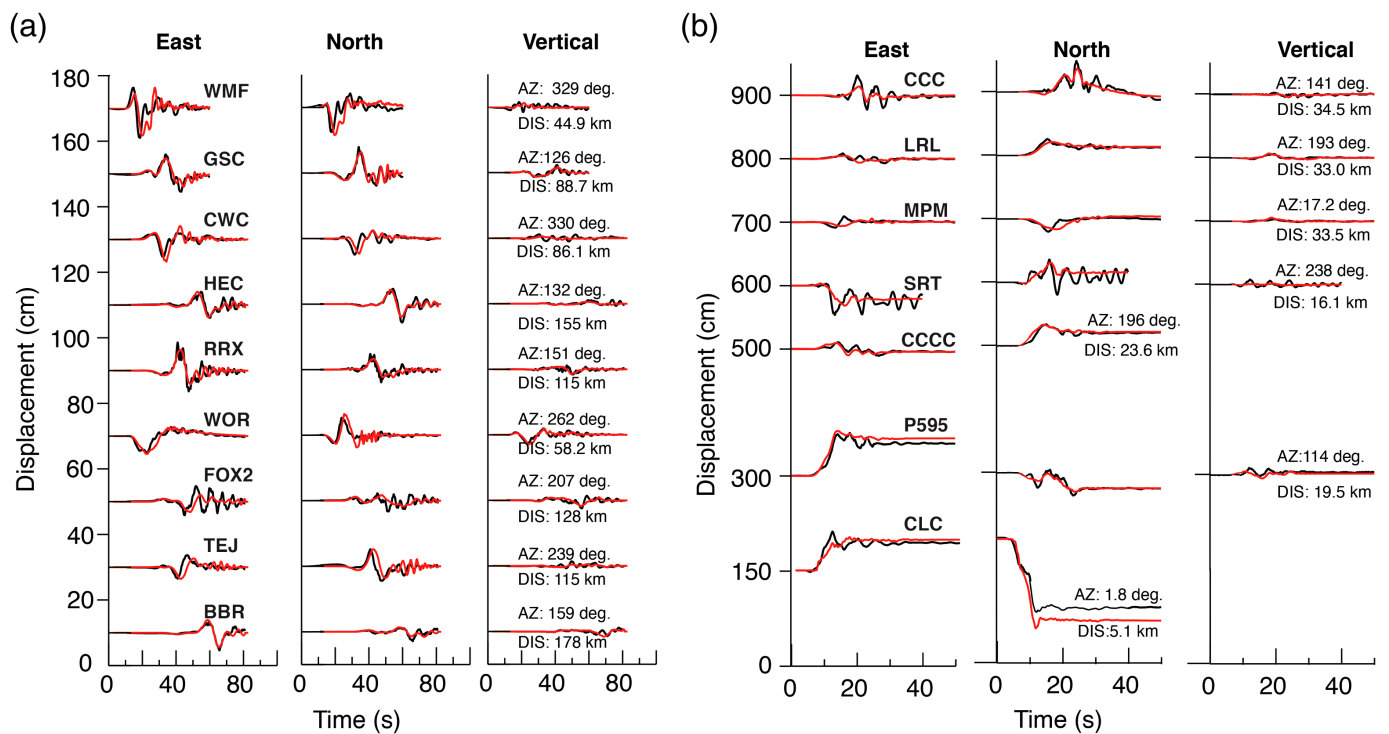
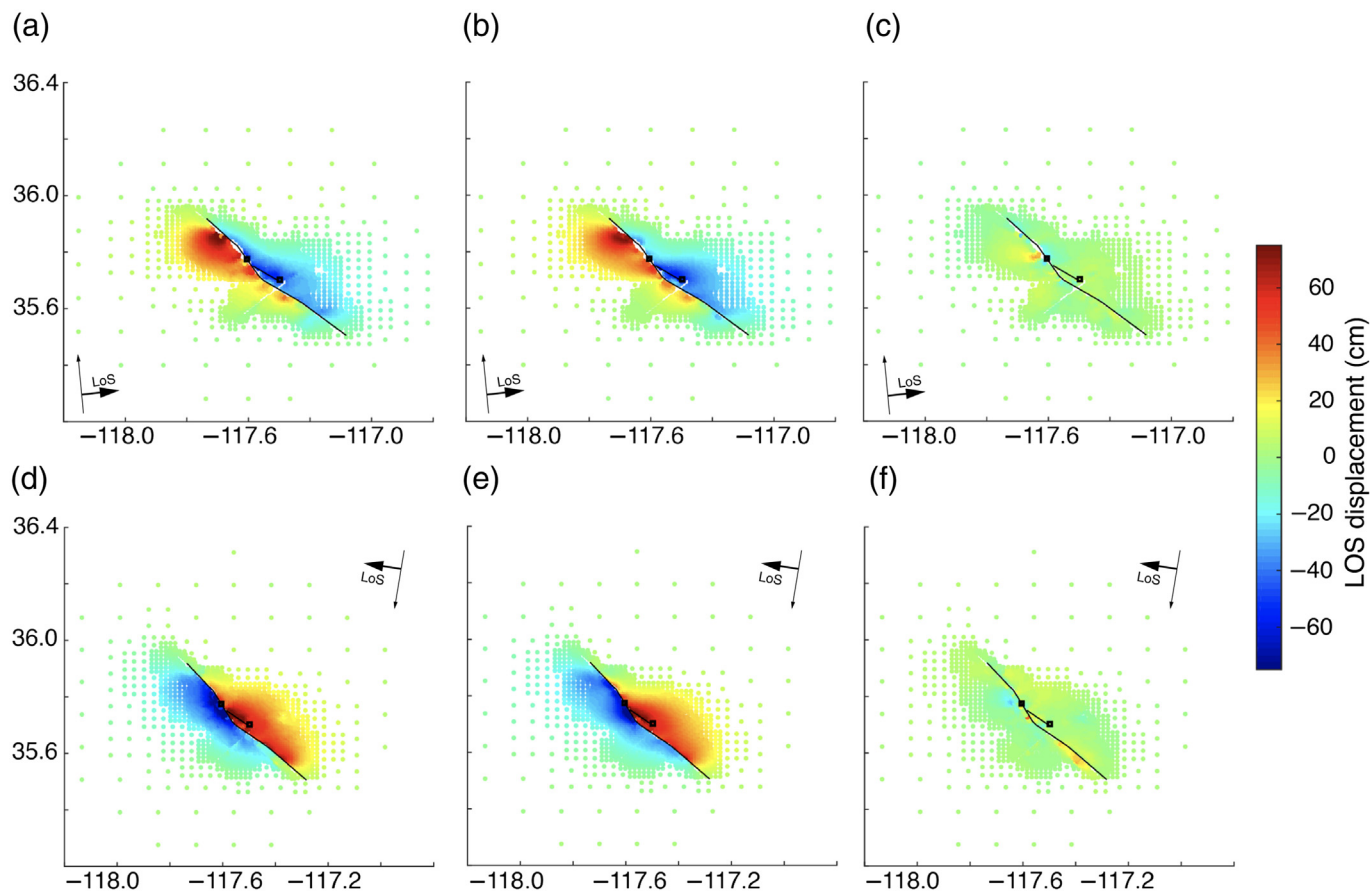


Figure 8. Observed (black) and modeled (red) displacement waveforms of the M_w 7.1 mainshock. Stations CCCC and P595 are from hr-Global Navigation

Satellite System (GNSS) observations. The color version of this figure is available only in the electronic edition.



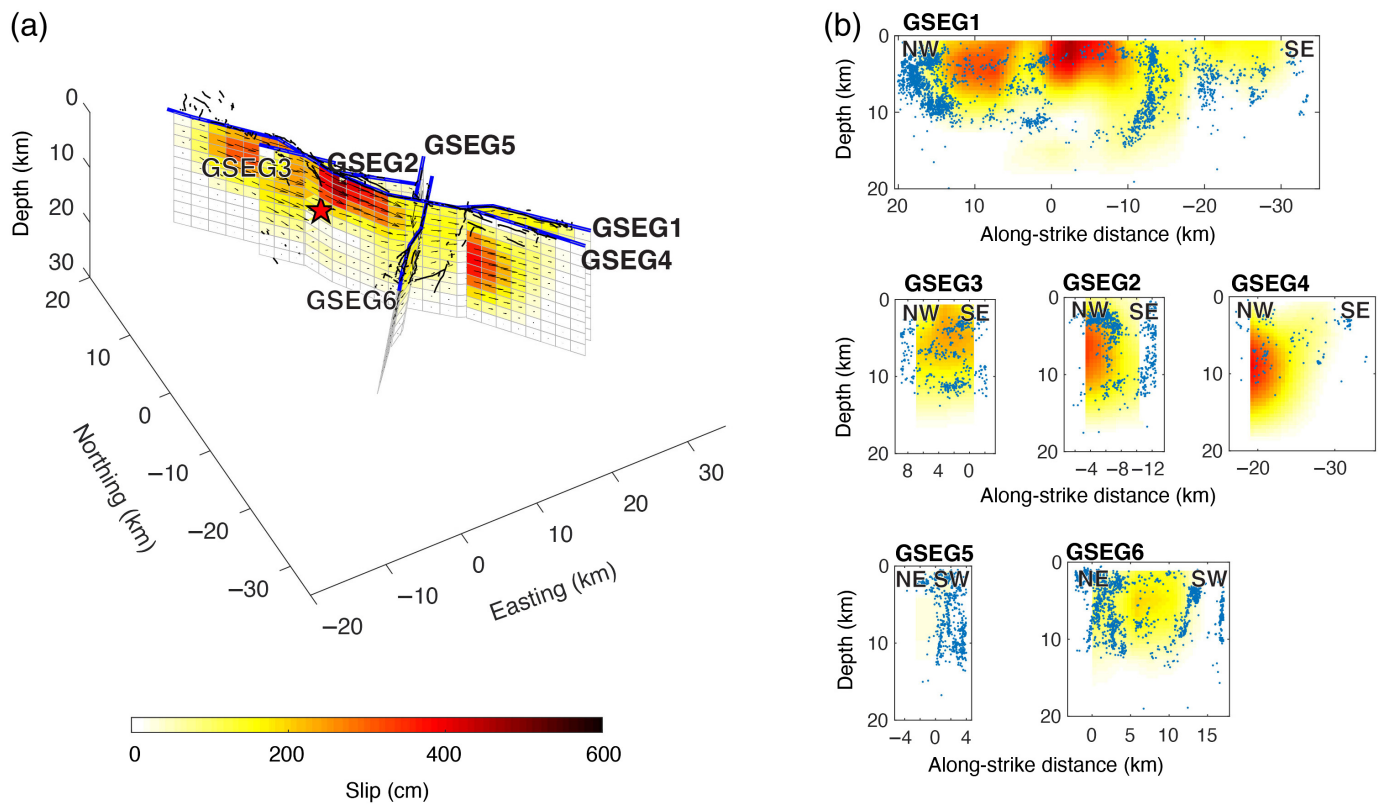
Geodetic inversion of both the events

To further illuminate the higher-order complexity of the 2019 Ridgecrest earthquake rupture, we also derive a coseismic slip model using InSAR and static GNSS data only (hereafter referred to as the geodetic-only model). Because the InSAR observations used in this study cover both the M_w 6.4 foreshock and the M_w 7.1 mainshock, in this exercise, we invert for the slip due to both events simultaneously. Compared to the joint inversions using both seismic and geodetic data, the geodetic-only model contains several more fault segments. In particular, we include one northwest-striking fault strand that runs subparallel to the southern half of the mainshock rupture (GSEG4 in Fig. 10a). Possible involvement of coseismic rupture along this fault segment is indicated by both the presence of surface fractures and lineation of aftershocks in this area (Fig. 1b). We include another northwest-striking spur northwest of the M_w 7.1 epicenter (GSEG3 in Fig. 10a). We also slightly modify the fault geometry adopted in the joint inversions, including the position and the strike of all fault segments, so that the top edges of the fault model better match the observed surface traces. Similar to the joint inversion, dip angles of the two segments that ruptured during the M_w 6.4 foreshock (GSEG2 and GSEG6) are determined by the aftershock distributions. The rest of the fault segments (GSEG1, GSEG3, GSEG4, and GSEG5) are assumed to be vertical, as

Figure 9. Sentinel-1 Interferometric Synthetic Aperture Radar (InSAR) line of sight (LoS) displacements. (a,d) The subsampled observations corrected for contributions from the foreshock, (b,e) the synthetic values, and (c,f) the residuals of the model fit. (a)–(c) The ascending Track ASC64 and (d)–(f) the descending track DES71. Black lines show the fault model, and the squares are the epicenters of the M_w 7.1 and M_w 6.4 events. The color version of this figure is available only in the electronic edition.

informed by the aftershock distributions, which show that except for the segment near the hypocenter, most aftershocks are symmetrically distributed with respect to the surface trace (Fig. S7).

We start the inversion in a uniform half-space medium and compute the Green's function using the Okada's dislocation formulas (Okada, 1985). The resulting slip model is shown in Figure S6. We then derive the slip model using a layered rigidity structure that is the same as the one used in the joint inversions. The resulting slip model is shown in Figure 10. Overall, the slip model based on a uniform half-space medium is similar to that based on the layered earth structure. One major difference is that the slip model based on a layered earth structure appears to have larger slip at greater depth, particularly around the junction between the M_w 6.4 and M_w 7.1 ruptures and the western segment at the southern end of the rupture (GSEG4). This feature is qualitatively consistent with



previous findings, which show that slip models based on a depth-increasing rigidity structure generally have larger slip at greater depth, compared to uniform half-space models (e.g. Fialko, 2004; Hearn and Bürgmann, 2005; Wang and Fialko, 2018). For the sake of consistency with the joint inversions, all descriptions and discussions in the following regarding the geodetic-only inversions refer to the slip model based on the layered rigidity structure.

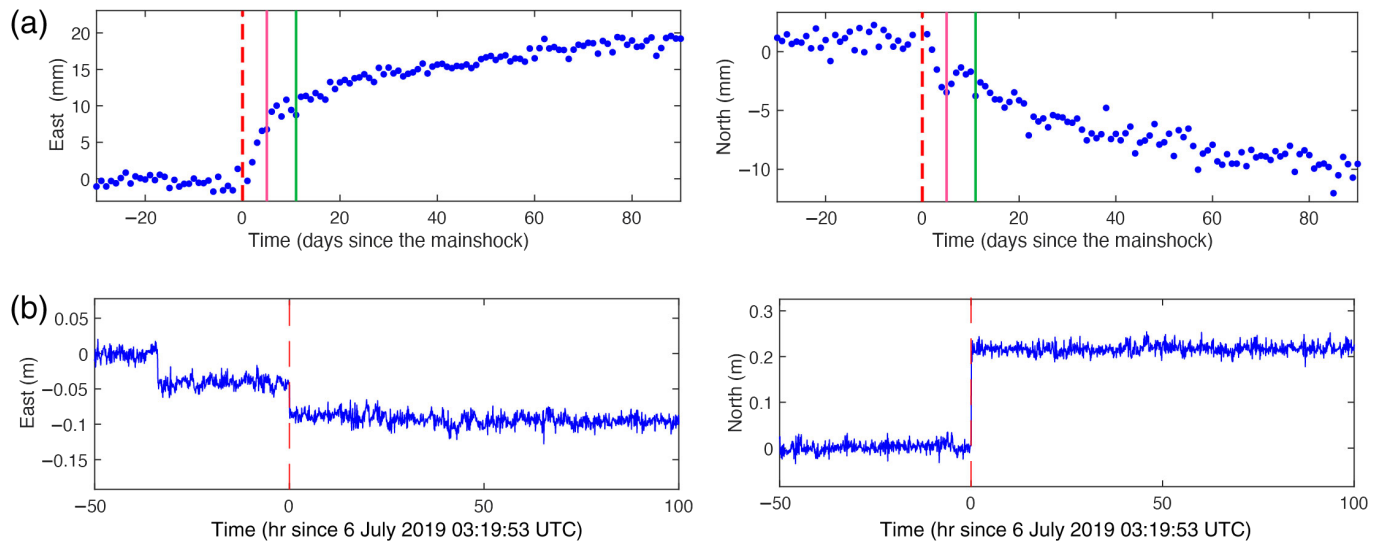
Similar to the joint inversion using both geodetic and seismic data (Figs. 6 and 7), our preferred geodetic-only model is also characterized by primarily right-lateral slip concentrated in three asperities along northwest-southeast-trending fault segments (GSEG1–4) and left-lateral slip along the southwest-northeast-trending fault strands (GSEG5–6) that are likely mainly involved in the M_w 6.4 foreshock. The overall distribution and magnitude of slip in the geodetic-only model is in close agreement with the joint inversion. Similar to the M_w 6.4 foreshock model (Fig. 2), most of the aftershocks a few days after the M_w 7.1 event occurred mainly around the areas of high coseismic slip (Fig. 10b). The most prominent slip peak occurs along a ~10 km long segment near the M_w 7.1 mainshock hypocenter, with a maximum slip of ~5 m, which is slightly smaller than that derived from joint inversion of both seismic and geodetic data.

As noted previously, slip on the northwest-striking spur GSEG2 during the M_w 6.4 foreshock is mostly concentrated in a depth range of 5–12 km, consistent with the inference of no clear surface rupture during the M_w 6.4 event along this

Figure 10. Coseismic slip model of the 2019 Ridgecrest earthquake sequence inverted from static GNSS and Sentinel-1 InSAR data. (a) Slip distribution in a 3D perspective. Black lines represent the surface traces of the 2019 Ridgecrest rupture verified by the USGS field survey (Ponti *et al.*, 2020). Solid blue lines represent the top edges of the slip model. (b) Slip distribution along average strike of the different fault segments. Dots are relocated aftershocks within 1 km from model surface trace during ~5 days after the M_w 6.4 foreshock on 4 July 2019 (Shelly, 2020). The color version of this figure is available only in the electronic edition.

segment (e.g., Milliner and Donnellan, 2020). Despite the potential smearing effect as a result of smoothing applied in the inversion, the geodetic-only slip model exhibits clear slip of >1 m near the surface on GSEG2. In addition, slip on this segment in the geodetic-only model is up to ~3 m, significantly larger than that obtained for just the M_w 6.4 foreshock (Fig. 10). These features suggest that this northwest-striking spur GSEG2 might have ruptured twice, with more pronounced and shallower slip during the M_w 7.1 mainshock (Wang and Bürgmann, 2020). Compared to the M_w 6.4 foreshock model, the concentration of slip on this fault strand in the geodetic-only model seems to be further to the north and closer to the M_w 7.1 hypocenter.

Although two subparallel fault strands at the southern end of the rupture are required to fit the sharp gradient in InSAR LoS displacements near the southern end of the rupture, particularly for the descending track DSC071 (Fig. 9), the slip on GSEG4, as shown in Figure. 10, seems to be unrealistically large. This could



be due to the close proximity of these two fault strands (the southernmost strand of GSEG1 and GSEG4), which may introduce a trade-off in slip between them, particularly at greater depth, in which the model resolution is expected to be low.

Another interesting feature is that near the M_w 7.1 hypocenter, the slip on the northeast spur GSEG2 is concentrated at a depth range of 4–10 km, which is noticeably deeper than that on the main rupture segment GSEG1, which has the maximum slip around a depth of 2–3 km. One possible scenario is that the main rupture fault GSEG1 in this part dips to the east and connects to the spur GSEG2 at depth. In fact, the model with an east-dipping segment near the M_w 7.1 hypocenter does slightly improve the InSAR data fitting around the fault (Fig. S9). The east-dipping fault geometry near the mainshock hypocenter is also consistent with the aftershock distribution, which illuminates an east-dipping structure near the junction of the main rupture trace and the northwest-striking spur at shallow depth and subvertical structure at deeper depth (profile C in Fig. S7). The complex surface ruptures, aftershock distribution, as well as the fault geometry inferred from the modeling of surface deformation, are overall consistent with a negative flower structure near the right-stepping releasing fault bend around the M_w 7.1 epicenter. A similar fault architecture has also been proposed by Ross *et al.* (2019) and Jin and Fialko (2020).

DISCUSSION

Contribution of early postseismic deformation

The second image of the Sentinel-1 interferograms used in this study was acquired a few days after the mainshock (on 10 July 2019 for the ascending track ASC064 and 16 July 2019 for the descending track DESC071, see Wang and Bürgmann, 2020, for details). To assess how much postseismic deformation may be included in the coseismic interferograms, we examine the GNSS time series at nearby stations. Figure 11 shows the time

Figure 11. GPS time series at station P595 showing only moderate postseismic deformation soon after the 2019 Ridgecrest earthquake. (a) Time series of daily solutions from one month before the M_w 7.1 to three months after. Magenta and green lines denote the time of the second image used to form the coseismic interferogram for the ascending track ASC064 and descending track DESC071, respectively. The pre-earthquake images of both tracks were acquired hours before the M_w 6.4 foreshock (\sim 18 : 51 Pacific Daylight Time (PDT) 3 July for ascending track ASC064 and \sim 06 : 52 PDT 4 July for descending track DESC071). The interseismic loading, seasonal variation, as well as the coseismic offsets due to both the M_w 6.4 foreshock and the M_w 7.1 mainshock have been corrected for. Note that the cumulative postseismic deformation during the first 10 days after the mainshock is less than 2 cm. (b) Time series of the 5 min solutions around the 2019 Ridgecrest earthquake sequence. Red dashed line represents the time of the M_w 7.1 mainshock. The PBO daily solutions are from Central Washington University and archived at UNAVCO. The 5 min solutions are from the Nevada Geodetic Laboratory (Blewitt *et al.*, 2018). The color version of this figure is available only in the electronic edition.

series of horizontal displacements around the time of the 2019 Ridgecrest earthquake at the closest station P595, which recorded the largest horizontal offset of \sim 570 mm during the M_w 7.1 mainshock (Wang and Bürgmann, 2020). Although there is a clear postseismic transient signal (Fig. 11a), both the daily and 5 min solutions show only modest deformation during the initial days after the mainshock. The cumulative postseismic displacement of P595 \sim 10 days after the mainshock is less than 15 mm, and there is no resolvable postseismic deformation in the 5 min time series during the first few days after the mainshock (Fig. 11b). This is in contrast to decimeter-level offsets estimated from 10 days of 1 Hz GNSS solutions from P595 by Goldberg *et al.* (2020), who concluded that a substantial fraction of the nominally coseismic Sentinel-1 LoS displacements was due to rapid postseismic deformation.

Nonetheless, the 2019 Ridgecrest earthquake sequence did indeed generate significant postseismic deformation during the

months after the mainshock. GNSS and Sentinel-1 observations from a few days after the earthquake to early September 2019 reveal up to ~ 5 cm postseismic deformation in a few localized areas around the M_w 7.1 mainshock and southwest of the fault junction of the M_w 6.4 and the M_w 7.1 main ruptures (Brooks *et al.*, 2020; Wang and Bürgmann, 2020). Preliminary analysis of the early postseismic near-field deformation suggests contributions from both afterslip and poroelastic rebound. Far-field GNSS data are consistent with large-scale deformation from deep-seated viscoelastic relaxation in the lower crust and upper mantle (e.g., Dorsett *et al.*, 2019; Pollitz *et al.*, 2019). Considering the modest amount of postseismic deformation captured by the GNSS time series of P595 and stations installed shortly after the earthquake (Brooks *et al.*, 2020), as well as the InSAR observations during several months after the mainshock (Wang and Bürgmann, 2020), we conservatively estimate that the early postseismic deformation contained in the coseismic interferograms amounts to less than 5% of the signal and probably does not exceed 5 cm, which is comparable to the uncertainty of the coseismic InSAR data.

Connection between the M_w 6.4 and the M_w 7.1 events

The Ridgecrest sequence began with a series of small earthquakes several hours preceding the M_w 6.4 event (magenta dots in Fig. 2b) distributed along a northwest-striking lineament northwest of its hypocenter (Huang *et al.*, 2019; Shelly, 2020). The M_w 6.4 event also generated abundant aftershocks that eventually illuminate a northwest-striking structure extending roughly from the M_w 6.4 epicenter to the M_w 7.1 epicenter (Ross *et al.*, 2019; Lomax, 2020; Shelly, 2020). The occurrence of the M_w 7.1 mainshock just ~ 34 hr after the M_w 6.4 event raises the question of how the occurrence of the M_w 7.1 mainshock is mechanically connected to the M_w 6.4 event. To explore this question, we compute the static coulomb stress change as well as the shear and normal stress changes imparted by the M_w 6.4 foreshock on the fault planes of the M_w 7.1 mainshock.

The coulomb stress change is defined as $\Delta\text{CFF} = \Delta\tau + \mu(\Delta\sigma - p)$, in which $\Delta\tau$ represents the shear stress change on the receiver fault plane projected onto the direction of potential slip; $\Delta\sigma$ the normal stress change on the fault plane and p the pore fluid pressure; μ the coefficient of friction, which is in the range of 0.6–0.8 for typical crustal rock. The sign convention here is that positive values of either $\Delta\tau$ or $\Delta\sigma$ would promote the potential fault slip. The effect of pore fluid pressure is equivalent to reducing the coefficient of friction; therefore, the equation of the coulomb stress change can be rewritten as $\Delta\text{CFF} = \Delta\tau + \mu'\Delta\sigma$, in which μ' represents the effective coefficient of friction when considering the pore pressure and $\mu' < \mu$. In this study, we assume $\mu' = 0.4$ (e.g., Freed, 2005).

In the modeling of the M_w 6.4 foreshock rupture process, we show that the majority of the moment release during this

event comes from slip on the southwest-striking fault strand (FSEG2 in Fig. 2), with only moderate slip on the northwest-striking strand (FSEG1 in Fig. 2). To explore the relative significance of stress change due to slip on these fault strands in triggering the M_w 7.1 mainshock, we first compute the stress change on the mainshock rupture planes due to the foreshock slip on the southwest-striking fault. We find that the slip on this fault produces overall negative stress change near the M_w 7.1 hypocenter (Fig. 12a). However, if slip on both of the fault segments (i.e., left-lateral slip on the southwest-striking fault and right-lateral slip on the northwest-striking spur) is considered, the M_w 6.4 earthquake produces a positive coulomb stress of up to ~ 0.5 MPa near the M_w 7.1 USGS hypocenter located at a depth of ~ 8 km, regardless of the coefficient of friction used, as both the normal stress, and the shear stress change near the M_w 7.1 hypocenter are positive (Fig. 12b). Notably, the coulomb stress increase at a shallower hypocentral depth of ~ 4 km as determined by Lomax (2020) and Lin (2020) is even higher, with a value up to ~ 1 MPa. This indicates that the slip on the northwest-striking spur is essential in triggering the M_w 7.1 mainshock, despite its relatively small magnitude of slip. The coulomb stress immediately southeast of the hypocenter is negative. The mainshock rupture propagation is bilateral on the main fault plane (MSEG1–4) as well as on the northeast spur (MSEG5). The slip on MSEG5 likely results in a dynamic stress perturbation on the main plane to the west (MSEG1 and 3) that overcomes the initial negative coulomb stress on that section. Figure 12 also shows that there is a large unclamping stress immediately north of the juncture between the foreshock southwest plane and the mainshock plane. It is in this region where the greatest mainshock slip occurred. An apparent correlation of peak slip zones and areas of prior static stress changes was also highlighted by Perfettini *et al.* (1999) for stress changes from two M_w 5.3–5.4 foreshocks of the 1989 Loma Prieta earthquake, by Parsons and Dreger (2000) for the Landers–Hector Mine earthquake sequence, and by Johanson and Bürgmann (2010) for the San Simeon–Parkfield earthquake sequence.

It is likely that the triggering relationship between the M_w 6.4 foreshock and the M_w 7.1 mainshock is more complex. Barnhart *et al.* (2019) show that in addition to the mainshock of the M_w 6.4 event, a few subsequent $M_w > 5$ aftershocks substantially contributed to the stress increase that eventually triggered the M_w 7.1 event. Rapid afterslip and/or other transient processes (e.g., postseismic fluid diffusion) following the M_w 6.4 event may also have played an important role in triggering the M_w 7.1 event (e.g. Huang *et al.*, 2019; Yue *et al.*, 2019).

Stress change on nearby faults

Large earthquakes are often followed by regional-scale seismicity variation, whose spatial distribution is often well correlated with the coulomb stress changes resulting from the mainshock (e.g., King *et al.*, 1994; Toda *et al.*, 2005; Freed, 2005).

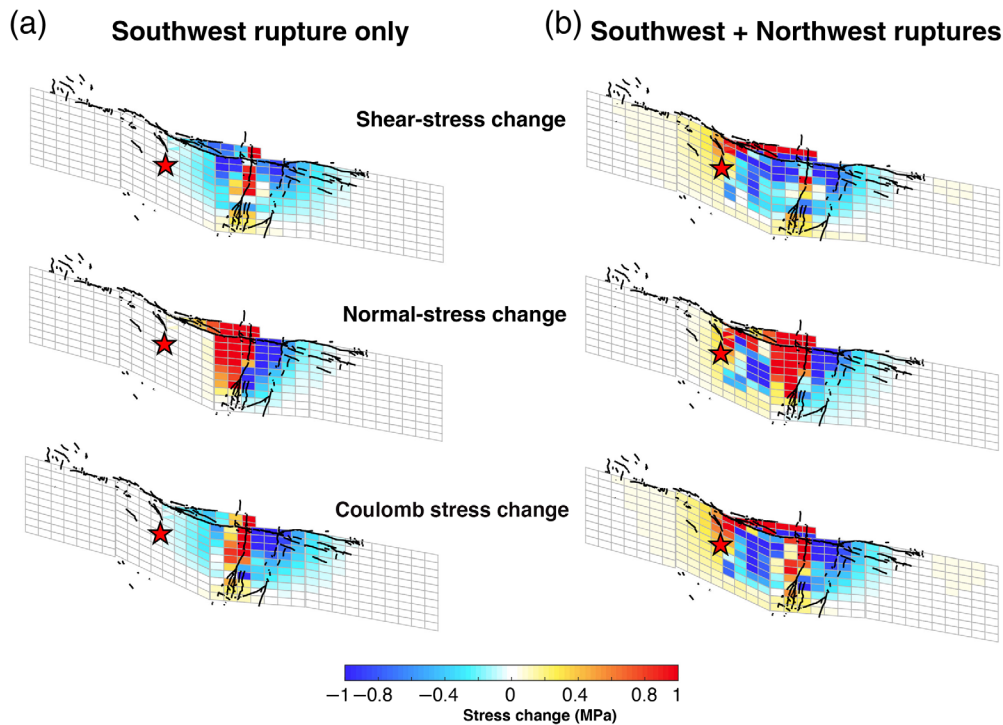


Figure 12. Stress perturbation on the M_w 7.1 rupture planes imparted by the M_w 6.4 foreshock. (a) Stress change due to slip on the southwest-striking fault only. (b) Stress change due to slip on both northwest-striking and the southwest-striking-fault strands. Effective coefficient of friction $\mu' = 0.4$ is used in the calculation. Red star represents the hypocenter of the M_w 7.1 mainshock. Positive values of all components of stress change encouraging the potential right-lateral slip. Fault geometry and subfault size (2 km \times 2 km) are the same as Figure 7. The color version of this figure is available only in the electronic edition.

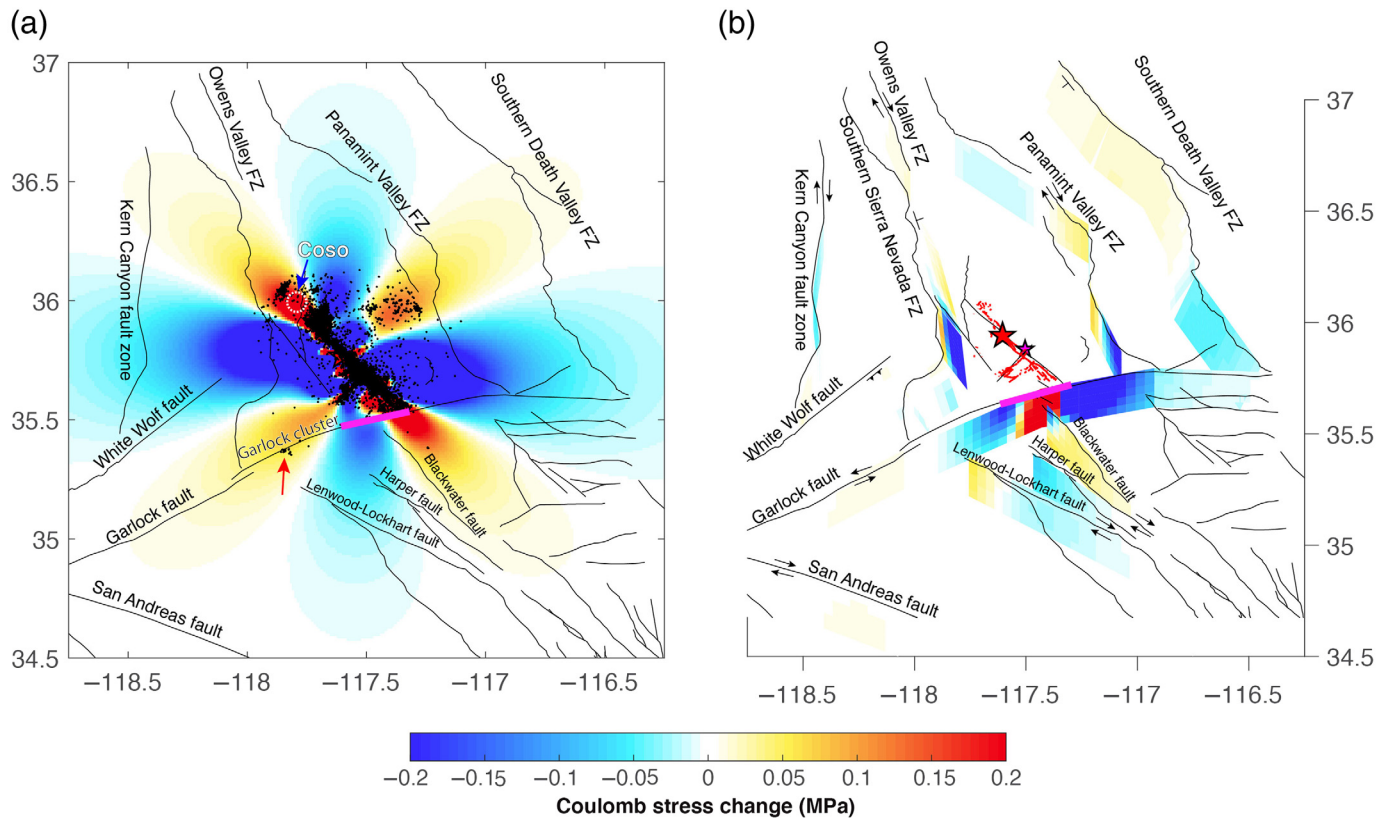
Spatiotemporal clustering and sequences of large events have also been linked to static stress interactions (e.g., Nalbant *et al.*, 1998; Parsons *et al.*, 2000; Freed *et al.*, 2007). To help assess the future regional seismic potential, we compute the coulomb stress change on nearby faults due to the 2019 Ridgecrest earthquake sequence. The calculation of coulomb stress depends on the orientation of the fault and the direction of the potential slip along which the stress tensor is projected (i.e., receiver fault). Except for the Garlock fault, which runs nearly east–westward and has a left-lateral sense of slip, most faults in the ECSZ around the 2019 Ridgecrest earthquakes strike northwest–southeastward and are characterized by right-lateral slip. For simplicity, here, we first compute the regional coulomb stress change assuming that all right-lateral and vertical receiver faults around the 2019 Ridgecrest earthquake sequence have a strike of 325° , similar to the geometry of the 2019 Ridgecrest mainshock rupture. Similar to the calculation for the stress interaction between the M_w 6.4 foreshock and the M_w 7.1 mainshock shown previously, we use an effective coefficient of friction $\mu' = 0.4$. The geodetic-only slip model shown in Figure 10 is used in this calculation.

Figure 13a shows the coulomb stress change around the 2019 Ridgecrest earthquake area calculated at a depth of 10 km.

As expected, areas immediately around the 2019 Ridgecrest ruptures experience a significant decrease in coulomb stress. At the two tips of the M_w 7.1 rupture, that is along the northern extension of the ECSZ fault zone to the north and the Blackwater fault to the south, the coulomb stress is increased by up to >0.2 MPa. Notably, the 24 January 2020 M_w 4.6 Barstow earthquake occurred along the southern end of the Blackwater fault. Another interesting observation is the elevated seismicity a few kilometers northwest of the Coso geothermal field starting several days after the mainshock (Fig. 13a). Spatially, this cluster of seismicity is located in the area of coulomb stress increase. Yet, similar to the relationship between the foreshock and mainshock, the temporal delay of this activity indicates that some other processes such as fluid diffusion might have also

played a role in triggering these earthquakes.

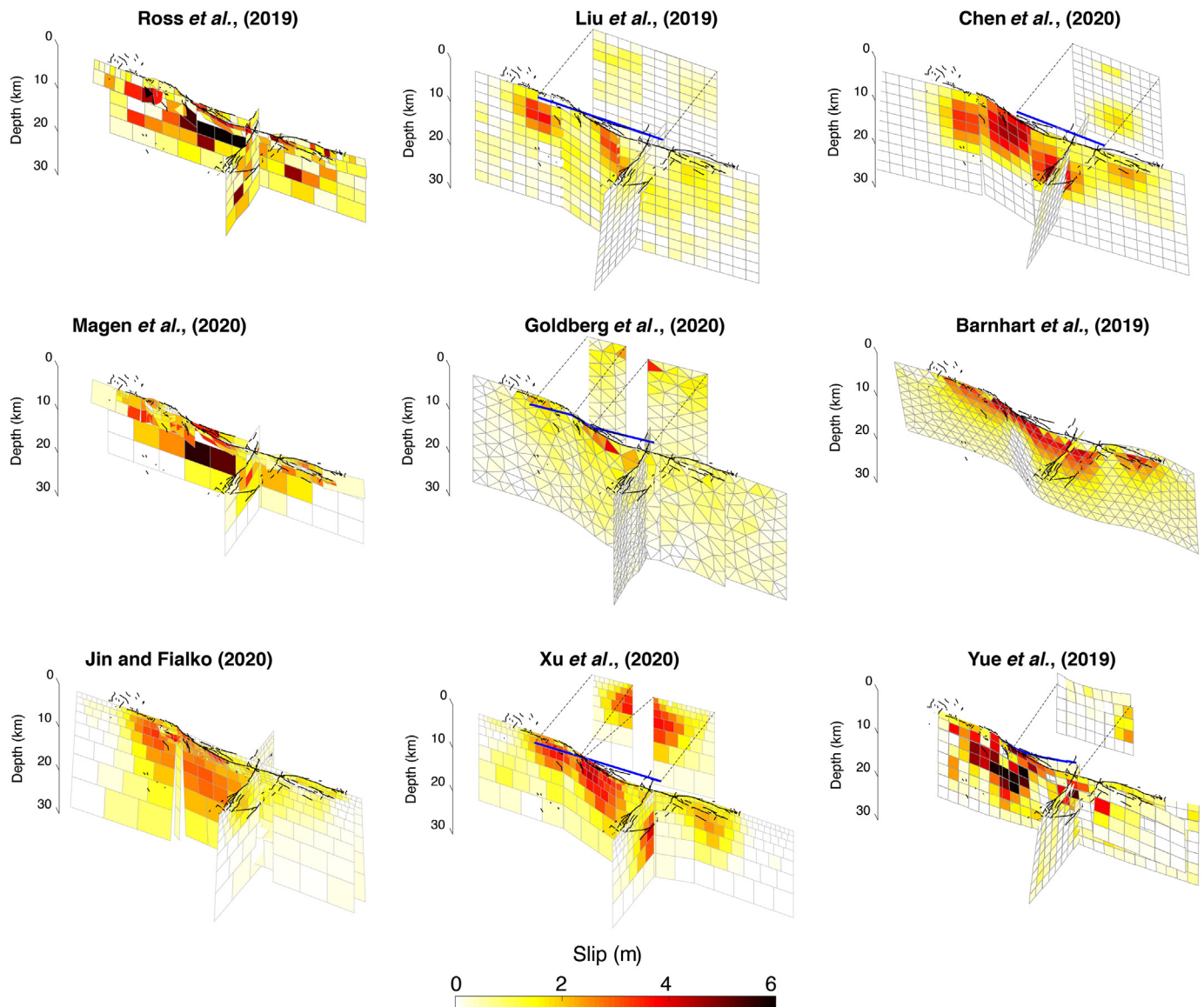
We also compute the coulomb stress change on individual major faults surrounding the 2019 Ridgecrest earthquake by projecting both the shear- and normal-stress components onto the respective slip directions of these faults across the entire seismogenic depth range from 0 to 20 km. The geometry and slip vectors of the respective faults are modified from the Southern California Earthquake Center Community Fault Model version 5.2 (Nicholson *et al.*, 2017). The results (Fig. 13b) are overall similar to the calculation assuming a uniform geometry for the receiver fault. However, we note that the calculation considering variable fault geometry should be more accurate, particularly for the left-lateral Garlock fault and the normal-faulting Southern Sierra Nevada fault zone. The most prominent coulomb stress increase is located along a ~ 20 km long section of the Garlock fault just southwest of the mainshock rupture termination, with a peak stress increase of ~ 0.5 MPa. The average interseismic shear strain along the Garlock fault at the surface is on the order of 50–100 nanostrain/yr (e.g., Shen *et al.*, 2007), which translates into a stress loading rate of 0.003–0.006 MPa/yr. Therefore, the coulomb stress increase on this segment of the Garlock fault due to the 2019 Ridgecrest sequence is equivalent to



the interseismic loading of at least 80 yr. This value is also at least three orders of magnitude higher than annual stress cycles from hydrological loading that have been shown to modestly modulate seismicity in California (Johnson *et al.*, 2017). East of the M_w 7.1 rupture, however, the coulomb stress change on the Garlock fault is clearly negative. The large coulomb stress changes on the Garlock fault segments immediately around the 2019 Ridgecrest earthquake sequence represent a combination of both shear- and normal-stress variations (Fig. S12a). Inspection of the normal stress component shows that the overall northwestward motion west of the M_w 7.1 rupture “unclamps” the Garlock fault, resulting in a coulomb stress increase on the segment immediately southwest of the M_w 7.1 rupture, whereas the section east of the M_w 7.1 rupture experiences “clamping.” Further to the west, between longitude 117.5 and 118 W, the Garlock fault sees coulomb stress decrease, due to negative shear stresses on this section (Fig. S12b). The section exposed to coulomb stress increase roughly coincides with the extent of triggered surface creep (Barnhart *et al.*, 2019; Ross *et al.*, 2019) and aftershock activity on the Garlock fault (Shelly, 2020). However, a cluster of small earthquakes between $\sim 117.75^\circ$ and 118° W several days after the 2019 Ridgecrest earthquake (e.g., Ross *et al.*, 2019; Hauksson *et al.*, 2020) seems to be within the zone of coulomb stress decrease, indicating that some other processes (e.g., dynamic triggering and poroelastic effects) might have been involved to trigger those events. In fact, these events are

Figure 13. Coulomb stress change on nearby faults induced by the 2019 Ridgecrest earthquake sequence. (a) Coulomb stress change computed on northwest-striking right-lateral receiver faults with strike = 325° and dip angle = 90° , at 10 km depth. Black dots show the relocated aftershocks through 25 July 2019 (Hauksson *et al.*, 2020). Red arrow marks the earthquake cluster on the Garlock fault days after the Ridgecrest earthquake (Ross *et al.*, 2019; Hauksson *et al.*, 2020). Magenta line marks the Garlock fault segment with triggered surface slip (Barnhart *et al.*, 2019; Ross *et al.*, 2019; Xu *et al.*, 2020). White dashed circle delineates the approximate extent of the Coso geothermal field. (b) Coulomb stress on several major faults surrounding the 2019 Ridgecrest earthquake. Positive values correspond to stress change promoting potential slip along the respective faults. An effective coefficient of friction is used in the calculations (corresponding shear- and normal-stress changes are shown in Fig. S10). The receiver fault model is modified from the Community Fault Model (CFM) version 5.2 (Plesch *et al.*, 2007; Nicholson *et al.*, 2017). Magenta and Red stars represent the M_w 6.4 foreshock and the M_w 7.1 mainshock epicenters, respectively. The color version of this figure is available only in the electronic edition.

along the section of positive normal-stress change (unclamping) (Fig. S12), which allows for fluid migration toward this section to further reduce the effective normal stress. The 2019 Ridgecrest earthquake sequence also produces a coulomb stress increase of ~ 0.02 MPa on the “big-bend” section of the San Andreas fault, which is equivalent to the interseismic loading of a few years, assuming an interseismic strain rate of ~ 200 nanostrain/yr.



Comparison of coseismic slip models

The rupture process of the 2019 Ridgecrest earthquake sequence has already been extensively studied using both geodetic and seismic observations. Several slip models have been published in the literature or recently submitted for publication (e.g. Barnhart *et al.*, 2019; Liu *et al.*, 2019; Ross *et al.*, 2019; Chen *et al.*, 2020; Goldberg *et al.*, 2020; Jin and Fialko, 2020; Magen *et al.*, 2020; Yue *et al.*, 2019; Xu *et al.*, 2020). In Figure 14, we show a comparison of several currently available source models in the same coordinate system and same 3D perspective view to highlight similarities and differences among these models. Interestingly, there are substantial differences in terms of both magnitude and slip distributions among many of these models. For example, the maximum slip in the model of Ross *et al.* (2019) is over 10 m, whereas only moderate peak slip of 2–3 m is obtained in the model of Goldberg *et al.* (2020). The spatial distribution of slip among these models is also remarkably different. The models of Ross

Figure 14. Comparison of coseismic models for the 2019 Ridgecrest earthquake sequence. All models are shown in the same coordinate system and 3D perspective view. The color version of this figure is available only in the electronic edition.

et al. (2019) and Yue *et al.* (2019) are characterized by highly heterogeneous slip on a limited number of patches at different locations. The models of Barnhart *et al.* (2019), Chen *et al.* (2020), Xu *et al.* (2020), and Jin and Fialko (2020), however, show relatively smooth slip variations across much of their respective fault models. Despite the differences, many of the models are characterized by a peak slip of 4–5 meter near the M_w 7.1 epicenter, with the second most prominent slip asperity located near the southern end of the rupture.

Table 3 summarizes the key observations and total moment release in the respective slip models. Except for Liu *et al.* (2019), all the models used Sentinel-1 InSAR observations.

TABLE 3

Comparison of Slip Models of the 2019 Ridgecrest Earthquake Sequence

Model	InSAR A: S1-A64, B: S1-D71, C: ALOS-2 D: CSK	Seismic Data	GNSS	Optical Imagery	Rigidity Structure Used in the Inversion	Moment (N-m)	Potency (m ³)
Ross <i>et al.</i> (2019)	A + B + C	N/A	Static	N/A	Layered	4.1×10^{19}	2.08×10^9
Liu <i>et al.</i> (2019)	N/A	Strong motion + teleseismic	Static	N/A	Layered	5.05×10^{19}	1.65×10^9
Chen <i>et al.</i> (2020)	A + B + C	Strong motion + teleseismic	Static + hr-GNSS	Sentinel-2 + PlanetLab	Layered	5.59×10^{19}	1.71×10^9
Magen <i>et al.</i> (2020)	A + B	N/A	Static	PlanetLab	Uniform half-space	4.96×10^{19}	1.42×10^9
Goldberg <i>et al.</i> (2020)	A + B	Strong motion	Static + hr-GNSS	N/A	Layered	4.85×10^{19}	1.49×10^9
Barnhart <i>et al.</i> (2019)	A + B	N/A	Static	Sentinel-2	Uniform half-space	5.39×10^{19}	1.54×10^9
Jin and Fialko (2020)	A + B + C + D	N/A	Static	N/A	Layered	6.79×10^{19}	1.94×10^9
Xu <i>et al.</i> (2020)	A + B	N/A	Static	PlanetLab	Uniform half-space	6.73×10^{19}	1.92×10^9
Yue <i>et al.</i> (2019)	A + B	Strong motion	Static + hr-GNSS	N/A	Layered	4.79×10^{19}	1.55×10^9
This study (joint inversion)	A + B	Strong motion	Static + hr-GNSS	N/A	Layered	5.20×10^{19}	2.44×10^9
This study (geodetic only)	A + B	No	Static	N/A	Layered	5.98×10^{19}	1.71×10^9

*The moment represents the combined value of both the M_w 6.4 foreshock and the M_w 7.1 mainshock. We note that both the moment and potency are subject to vary depending on the smoothing constraint in the inversion, and the moment strongly depends on the assumed rigidity structure. For the models derived with geodetic data only (Barnhart *et al.*, 2019; Jin and Fialko, 2020; Magen *et al.*, 2020; Xu *et al.*, 2020; and the geodetic-only model of this study), the moment is computed with a nominal shear modulus of 35 GPa, even though some models are based on a layered rigidity structure. This is because geodetic slip inversions are less sensitive to the shear modulus; a reasonable variation in shear modulus can thus result in a large variation in estimated moment, even while surface deformation and the resulting slip distribution remain similar. Moment values of other studies are either taken from the respective publications or the authors. CSK, Cosmo–SkyMed InSAR; GNSS, Global Navigation Satellite System; hr-GNSS, high-rate Global Navigation Satellite System; InSAR, Interferometric Synthetic Aperture Radar; N/A, not applicable; S1-A64, Sentinel-1 InSAR from the ascending track ASC064; S1-D71, Sentinel-1 InSAR from the descending track DSC071.

Figure S10 compares the model predictions from different slip models with the Sentinel-1 observations from Wang and Bürgmann (2020). Not surprisingly, the models derived from only geodetic data (i.e., Jin and Fialko, 2020; Magen *et al.*, 2020; Xu *et al.*, 2020; and geodetic-only model of this study) generally fit the Sentinel-1 InSAR data better. Misfits between the observations and model predictions by some models, however, exceed 30 cm over a wide area, which is significantly higher than the expected noise level of 2–3 cm in the Sentinel-1 data (Wang and Bürgmann, 2020).

We note that the comparison here is not meant to judge which model is better than others, because many factors, including the fault geometry, model parameterization, data selection, regularization, and the calculations of Green's functions in the inversion could affect the resulting slip model. Rather, it is provided to document the variability in such inversions and provide insight into the uncertainties in slip inversions. As shown in Figure 14 and Table 3, both the fault geometry and the data used in those studies are different to certain degrees, which would inevitably produce differences in the resulting slip models and data fitting for a given data type. Nevertheless, we hope that this comparison is informative for assessing how well we can currently resolve the rupture process of as complex an earthquake as the 2019 Ridgecrest earthquake sequence.

Shallow slip deficit

Inversions of high-quality geodetic data from several $\sim M_w$ 7 continental strike-slip earthquakes, including the 1992 M_w 7.3 Landers, the 1999 M_w 7.1 Hector Mine, the 1999 M_w 7.5 İzmit, and the 2010 M_w 7.2 El Mayor–Cucapah ruptures (Simons *et al.*, 2002; Cakir *et al.*, 2003; Fialko, 2004; Huang *et al.*, 2017), show that the maximum moment release during these earthquakes occurs in the middle of the seismogenic layer between 3 and 6 km, and the slip in the uppermost few kilometers (0–3 km) is systematically less than that at greater depth. This reduction of the coseismic slip in the uppermost part of the elastic crust is referred to as the shallow slip deficit (SSD) expressed as the percentage of reduction in mean shallow slip versus peak mean slip at depth (Fialko *et al.*, 2005).

The inferred SSD for several of the aforementioned events is as high as 60% (Kaneko and Fialko, 2011). However, Xu *et al.* (2016) and Huang *et al.* (2017) show that depending on the data completeness, particularly close to the fault, and the degree of smoothing and/or other regularization in the inversion, the estimation of the SSD can be significantly biased. In this study, we have collected slip models from different groups with different datasets and inversion strategies. These models offer us a unique opportunity to examine to what degree we can resolve the SSD for the 2019 Ridgecrest earthquake.

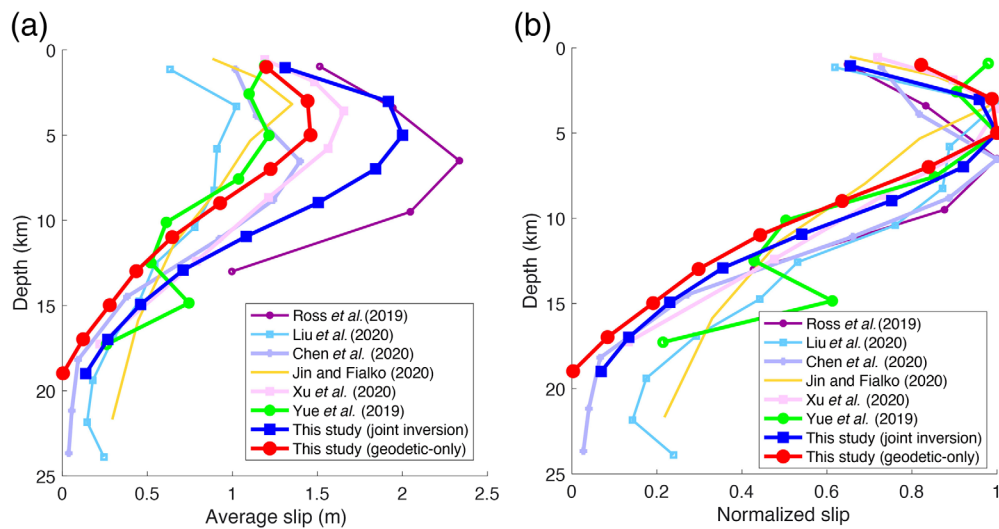


Figure 15. Profile of slip as a function of depth. (a) Average slip versus depth of different slip models. (b) Normalized slip as a function of depth. Only models with rectangular fault patches are included in this comparison. The model by Magen *et al.* (2020) is not included, because their model rupture has only three layers. The color version of this figure is available only in the electronic edition.

Here, we first estimate the average slip in each depth range, which is defined as

$$\bar{S}_i = \frac{\sum_i L_i W_i S_i}{\sum_i L_i W_i},$$

in which S_i , L_i , and W_i represent the slip, length, and width of corresponding fault patches in depth range, respectively. Because the models we collected have varying fault discretization, patch layers, and information detailing the model geometry, to ensure a consistent comparison, we group the patches in each model into a given number of clusters, according to the depth of the corresponding patches. The number of clusters is chosen as the maximum number of layers in each model. We perform the cluster analysis using the k-means algorithm in MATLAB (see [Data and Resources](#)).

Figure 15a shows the average slip as a function of depth for the models with rectangular patches. Except for the model by Yue *et al.* (2019), all models are characterized by relatively smaller slip close to the surface, and the maximum average slip occurs in the depth range from 3 to 8 km. The maximum average slip of these profiles varies over a wide range, from ~ 1 m in the model by Liu *et al.* (2019) to >2 m in the model by Ross *et al.* (2019). We note that the estimation of average slip in each depth range depends on the along-strike extent of the fault model and smoothness of the corresponding slip model. To have a more consistent comparison of SSD in these models, we normalize the slip versus depth profile by its maximum average slip in each model. The results are shown in Figure 15b. Despite the large variance, all models except the

one by Yue *et al.* (2019) show a clear SSD of as much as $\sim 40\%$. As noted previously, the 2019 Ridgecrest earthquake is well imaged by both InSAR and optical imagery observations. In particular, the Sentinel-1 observations from both satellite tracks preserve relatively high radar coherence near the surface rupture (Wang and Bürgmann, 2020). Thus, a lack of data completeness near the fault is not likely to introduce a significant overestimate of the SSD (e.g., Xu *et al.*, 2016). Although the models we collected have different degrees of smoothing (Fig. 14), the SSD is a common feature, suggesting that there is a significant SSD during the 2019 Ridgecrest

earthquake. However, we note that the magnitude of the SSD from these models is quite variable, ranging from $\sim 40\%$ in the model by Jin and Fialko (2020) and the joint-inversion model of this study to nearly 0% in Yue *et al.* (2019), suggesting that the inversion procedure and data selection can indeed substantially affect estimates of the SSD. Combining all models collected in this study, we conclude that the average SSD during the 2019 Ridgecrest earthquake sequence is $\sim 20\%$ – 30% , similar to the Landers but greater than for Hector Mine and the El Mayor–Cucapah ruptures (Xu *et al.*, 2016; Huang *et al.*, 2017).

Mechanisms proposed to explain the geodetically inferred SSD include: (1) interseismic creep and afterslip as a result of velocity strengthening rock friction in the shallow crust (e.g., Scholz, 1998; Johanson *et al.*, 2006; Barbot *et al.*, 2012; Floyd *et al.*, 2016), (2) the effect of a damage or compliant fault zone that is not considered in the inversion (Fialko *et al.*, 2005; Barbot *et al.*, 2008), and (3) off-fault elastoplastic deformation (Kaneko and Fialko, 2011; Milliner *et al.*, 2015). The SSD has also been associated with immature or incipient faults (e.g., Xu *et al.*, 2016; Li *et al.*, 2020), in which the rupture features macroscopic complexity, and a significant portion of shallow coseismic deformation is more broadly distributed. Furthermore, Lauer *et al.* (2020) recently suggested that the SSD may be magnitude dependent.

Although these models can explain the development of an SSD, the ambient stress field and the recent slip history of a fault may also affect the depth dependence of slip during a large earthquake. For the 2019 Ridgecrest earthquake, we note that, near the M_w 7.1 mainshock epicenter, the

maximum slip is quite close to the surface, although the average slip peaks at 3–8 km depth. If the SSD is controlled by the same mechanism, one might expect a more uniform reduction in slip toward the surface, assuming that the physical properties of the fault zone do not vary significantly along strike. However, the stress field may be highly heterogeneous due to the spatiotemporal complexity of faulting and stress evolution in the crust (e.g., [Smith and Heaton, 2011](#)). It is possible that some sections of the fault experience a low magnitude of slip near the surface, whereas other sections may have slip excess, depending on the previous fault slip history on and near the eventual rupture.

Low-rupture velocity and the immaturity and complexity of the faults

The foreshock and mainshock models retrieved in this study by joint inversion of seismic and geodetic datasets are characterized by relatively low rupture velocity values (Table 2). Despite the differences among kinematic models published in the literature and shown in Figure 14, a low-rupture velocity is a common feature of all the rupture histories inferred from modeling the seismic waveform data. Specifically, [Liu et al. \(2019\)](#) found an unusually low-rupture velocity of 1.0–1.5 km/s for both the foreshock and mainshock, and interpreted this as the result of rupture on a relatively immature fault system. [Ross et al. \(2019\)](#) and [Chen et al. \(2020\)](#) also found that the mean rupture velocity of the 2019 Ridgecrest earthquake sequence was ~ 2 km/s and suggested that the rupture process of Ridgecrest earthquakes could represent a cascading progression in a highly segmented fault system. [Goldberg et al. \(2020\)](#) attributed similarly low-velocity values to be indicative of immature fault systems, which are geometrically more complex and rougher than their more developed counterparts (e.g., [Perrin et al., 2016](#)). In this study, rupture-velocity values for the foreshock and mainshock range between 1.9 and 2.5 km/s (Table 2).

It is important to note that the definition of high or low values of rupture velocity is related to the velocity models that the various authors used to compute their Green's functions. The model adopted in this study has a shallow layer with a relatively slow shear-wave velocity of 2.0 km/s that was needed to better fit the shear-wave and surface-wave arrivals in the local to regional distance data. The shallowest slip retrieved on the southwest-striking fault plane during the foreshock has a rupture velocity of 1.9 km/s, which allows the propagation to be subshear up to the surface. For the mainshock, the maximum allowed rupture velocity of 2.2 km/s is at least 67% of the shear-wave velocity over the depth range with most of the slip between 2 and 10 km depth. Although the ratio of rupture to shear velocity increases in the shallowest row of subfaults, evidence from the kinematic model (see animation in the supplemental material) indicates that the rupture was locally delayed, and there was significant slip accumulation after the passage of

the rupture front. This indicates a slower rupture velocity and longer rise time (lower slip velocity) at shallow depth as well as at the juncture between MSEG1 and MSEG3.

Theoretical dynamic models suggest that the rupture velocity of a propagating front is controlled by geometrical complexities, fault roughness, frictional properties, stress-field heterogeneities, among many other factors ([Oglesby and Mai, 2012](#); [Fang and Dunham, 2013](#), [Wollherr et al., 2019](#)). In particular, an inverse proportionality between rupture velocity and fracture energy has been found in theoretical models ([Day, 1982](#); [Andrews, 1976](#); [Ohnaka and Yamashita, 1989](#); [Rice et al., 2005](#), among many others). Even though we cannot associate the inferred low-rupture velocity to one specific cause, we speculate that the high values of fracture energy required to allow the slip pulse to propagate through the geometrical complexity reduced the directivity effects in the rupture propagation and potentially limited the magnitude of both the events.

CONCLUSIONS

Consisting of two major events, the 4 July M_w 6.4 foreshock and the 6 July M_w 7.1 mainshock, the 2019 Ridgecrest earthquake sequence culminated in the largest seismic event in California, since the 1992 M_w 7.3 Landers and the 1999 M_w 7.1 Hector Mine earthquakes. It ruptured a complex array of intersecting faults in a region of active deformation and seismicity in the ECSZ. Rupture of the M_w 6.4 foreshock started on a northwest-striking right-lateral fault strand and then continued on a southwest-striking fault with mainly left-lateral slip. Slip on the northwest-striking fault strand seems to have played a more important role than the southwest-striking fault in triggering the M_w 7.1 mainshock ~ 34 hr later, even though most of the moment release of the M_w 6.4 foreshock was along the southwest-striking fault. Notably, the coulomb stress increase in the mainshock hypocentral area is largely controlled by the slip on the northwest-striking plane of the foreshock. Aftershocks and afterslip may have further contributed to the delayed triggering of the mainshock. The rupture of the M_w 7.1 mainshock is characterized by dominantly right-lateral slip on a series of northwest-striking fault strands, including the one that had already been activated during the nucleation of the M_w 6.4 foreshock. The maximum slip of the M_w 7.1 event is ~ 5 m, at a depth range of 3–8 km. Most early aftershocks in the days following the ruptures are distributed surrounding fault areas of high-coseismic slip. Both the M_w 6.4 foreshock and M_w 7.1 mainshock are characterized by a relatively low-rupture velocity of ~ 2 km/s, which is possibly related to the geometric complexity and immaturity of faults in the ECSZ.

Despite the good coverage of both geodetic and seismic observations in southern California, published coseismic slip models of the 2019 Ridgecrest earthquake sequence show large variations, which are likely due to the different choices in datasets, fault parameterization, regularization, as well as

the assumed rigidity structure in these inversions. These large variations highlight the real uncertainty of earthquake rupture inversions that are nowadays routinely performed for large earthquakes. Nonetheless, most of the slip models we compare in this study are characterized by a SSD of ~20%–30%. In addition to the previously proposed mechanisms proposed to explain the SSD, we suggest that the ambient stress field and previous slip history may also locally affect the depth distribution of coseismic slip during a large earthquake.

The 2019 Ridgecrest earthquake sequence produced a significant coulomb stress change on the nearby fault networks. In particular, the Garlock fault segment southwest of the M_w 7.1 rupture experienced a coulomb stress increase of ~0.5 MPa, equivalent to the interseismic loading of a few decades. Large coulomb stress increase here might be responsible for the triggered surface creep on the Garlock fault during the 2019 Ridgecrest earthquake sequence. Except for the narrow band of events in close vicinity of the rupture, most aftershocks are distributed in areas of coseismic coulomb stress increase. Analysis of continuous GNSS time series at nearby stations and postseismic InSAR observations several months after the mainshock suggest that the coseismic interferograms used in this study contain only modest amounts (<5 cm) of postseismic deformation. Detailed coseismic slip models as derived in this study will be useful to study the postseismic relaxation following the 2019 Ridgecrest earthquake sequence.

DATA AND RESOURCES

Static Global Navigation Satellite System (GNSS) coseismic displacements are available at <http://sopac-csrc.ucsd.edu/index.php/ridgecrestjuly2019> (last accessed March 2020). The Global Centroid Moment Tensor (Global CMT) Project database was searched using www.globalcmt.org/CMTsearch.html (last accessed October 2019). The Global CMT moment tensor solution of the M_w 6.4 foreshock is available at <http://ds.iris.edu/spud/momenttensor/17664799> (last accessed March 2020). The California Integrated Seismic Network (CISN) solution of the M_w 6.4 foreshock epicenter is available at <https://earthquake.usgs.gov/earthquakes/eventpage/ci38443183/executive> (last accessed March 2020). Description of the Western United States (WUS) seismicity velocity model is available at http://www.eas.slu.edu/eqc/eqc_mt/MECH.NA/20190704173349/index.html (last accessed March 2020). Information about the January 2020 M_w 4.6 Barstow, California, earthquake is available at <https://earthquake.usgs.gov/earthquakes/eventpage/ci39281440/executive> (last accessed March 2020). Additional figures illustrating the method of joint inversion and data fitting of different slip models are included in the supplementary material. Slip model derived in this study can be retrieved from <http://seismo.berkeley.edu/~burgmann/research.html> (last accessed June 2020). The MATLAB is available at <https://www.mathworks.com/help/stats/kmeans.html> (last accessed June 2020).

ACKNOWLEDGMENTS

The authors thank David Shelly and Hui Huang for sharing their relocated earthquake catalogs. This work benefited from discussions with Baptiste Rousset, Chris Milliner, Zach Ross, Zeyu Jin, Yuri Fialko,

Xiaohua Xu, Han Yue, Chen Ji, and many others at the Southern California Earthquake Center (SCEC) 2019 annual meeting and American Geophysical Union (AGU) 2019 fall meeting. The insightful comments and suggestions from Guest Editor Sue Hough and Reviewers Anthony Lomax and Arben Pitarka helped improve the article. Roland Bürgmann and Kang Wang acknowledge support from the National Aeronautics and Space Administration (NASA) Earth Surface and Interior Program (NNX16AL17G) and the SCEC. The authors thank all authors who shared their slip models.

REFERENCES

- Amos, C. B., S. J. Brownlee, D. H. Rood, G. B. Fisher, R. Bürgmann, P. R. Renne, and A. S. Jayko (2013). Chronology of tectonic, geomorphic, and volcanic interactions and the tempo of fault slip near Little Lake, California, *Geol. Soc. Am. Bull.* **125**, 1187–1202, doi: [10.1130/B30803.1](https://doi.org/10.1130/B30803.1).
- Andrews, D. J. (1976). Rupture velocity of plane strain shear cracks, *J. Geophys. Res.* **81**, no. 32, 5679–5687.
- Barbot, S., N. Lapusta, and J.-P. Avouac (2012). Under the hood of the earthquake machine: Toward predictive modeling of the seismic cycle, *Science* **336**, 707–710, doi: [10.1126/science.1218796](https://doi.org/10.1126/science.1218796).
- Barbot, S., Y. Fialko, D. Sandwell, and D. Sandwell (2008). Effect of a compliant fault zone on the inferred earthquake slip distribution, *J. Geophys. Res.* **113**, no. B06404, doi: [10.1029/2007JB005256](https://doi.org/10.1029/2007JB005256).
- Barnhart, W. D., G. P. Hayes, and R. D. Gold (2019). The July 2019 Ridgecrest, California, earthquake sequence: Kinematics of slip and stressing in cross-fault ruptures, *Geophys. Res. Lett.* **107**, no. 3, 1240–1249, doi: [10.1029/2019gl084741](https://doi.org/10.1029/2019gl084741).
- Benetatos, C., D. Dreger, and A. Kiratzi (2007). Complex and segmented rupture associated with the 14 August 2003 M_w 6.2 Lefkada, Ionian Islands, earthquake, *Bull. Seismol. Soc. Am.* **97**, 35–51.
- Blewitt, G., W. C. Hammond, and C. Kreemer (2018). Harnessing the GPS data explosion for interdisciplinary science, *EOS* **99**, 1–2, doi: [10.1029/2018EO104623](https://doi.org/10.1029/2018EO104623).
- Brooks, B., J. Murray, J. A. Svarc, E. A. Phillips, R. A. Turner, M. H. Murray, T. Ericksen, K. Wang, S. Minson, R. Bürgmann, *et al.* (2020). Rapid geodetic observations of spatiotemporally varying postseismic deformation following the Ridgecrest earthquake sequence: The U.S. Geological Survey response, *Seismol. Res. Lett.* doi: [10.1785/0220200007](https://doi.org/10.1785/0220200007).
- Cakir, Z., J. B. D. Chabaliere, R. Armijo, B. Meyer, A. Barka, and G. Peltzer (2003). Coseismic and early post-seismic slip associated with the 1999 Izmit earthquake (Turkey), from SAR interferometry and tectonic field observations, *Geophys. J. Int.* **155**, no. 1, 93–110.
- Carlson, C. W., C. J. Pluhar, J. M. G. Glen, and M. J. Farner (2013). Kinematics of the west-central walker lane: Spatially and temporally variable rotations evident in the late miocene stanislaus group, *Geosphere* **9**, no. 6, 1530–1551, doi: [10.1130/GES00955.1](https://doi.org/10.1130/GES00955.1).
- Chen, K., J.-P. Avouac, S. Aati, C. Milliner, F. Zheng, and C. Shi (2020). Cascading and pulse-like ruptures during the 2019 Ridgecrest earthquakes in the eastern California shear zone, *Nat. Commun.* **11**, no. 1, 313, doi: [10.1038/s41467-019-13750-w](https://doi.org/10.1038/s41467-019-13750-w).
- Day, S. M. (1982). Three-dimensional simulation of spontaneous rupture: The effect of nonuniform prestress, *Bull. Seismol. Soc. Am.* **72**, 1881–1902.

- Dixon, T. H., E. Norabuena, and L. Hotaling (2003). Paleoseismology and Global Positioning System: Earthquake-cycle effects and geotectonic versus geologic fault slip rates in the eastern California shear zone, *Geology* **31**, no. 1, 55–58, doi: [10.1130/0091-7613\(2003\)031<0055:PAGPSE>2.0.CO;2](https://doi.org/10.1130/0091-7613(2003)031<0055:PAGPSE>2.0.CO;2).
- Dorsett, J., K. Johnson, S. Puel, and T. W. Becker (2019). Postseismic deformation and stress evolution following the 2019 M 7.1 and M 6.4 Ridgecrest earthquakes, *AGU Fall Meeting Abstract*, S31G-0500.
- Dreger, D., R. Uhrhammer, M. Pasyanos, J. Franck, and B. Romanowicz (1998). Regional and far-regional earthquake locations and source parameters using sparse broadband networks: A test on the Ridgecrest sequence, *Bull. Seism. Soc. Am.* **88**, 1353–1362.
- Dreger, D. S., M. H. Huang, A. Rodgers, T. Taira, and K. Wooddell (2015). Kinematic finite-source model for the 24 August 2014 South Napa, California, earthquake from joint inversion of seismic, GPS and InSAR data, *Seismol. Res. Lett.* **86**, 327–334, doi: [10.1785/0220140244](https://doi.org/10.1785/0220140244).
- Dreger, D. S., D. D. Oglesby, R. A. Harris, N. Ratchkovski, and R. Hansen (2004). Kinematic and dynamic rupture models of the November 3, 2002 M_w 7.9 Denali, Alaska, earthquake, *Geophys. Res. Lett.* **31**, L04605, doi: [10.1029/2003GL018333](https://doi.org/10.1029/2003GL018333).
- Ekström, G., M. Nettles, and A. M. Dziewoński (2012). The Global CMT project 2004–2010: Centroid-moment tensors for 13,017 earthquakes, *Phys. Earth Planet. In.* **200/201**, 1–9, doi: [10.1016/j.pepi.2012.04.002](https://doi.org/10.1016/j.pepi.2012.04.002).
- Fang, Z., and E. M. Dunham (2013). Additional shear resistance from fault roughness and stress levels on geometrically complex faults, *J. Geophys. Res.* **118**, 3642–3654, doi: [10.1002/jgrb.50262](https://doi.org/10.1002/jgrb.50262).
- Fialko, Y. (2004). Probing the mechanical properties of seismically active crust with space geodesy: Study of the coseismic deformation due to the 1992 M_w 7.3 Landers (southern California) earthquake, *J. Geophys. Res.* **109**, no. B002756, 1–19, doi: [10.1029/2003JB002756](https://doi.org/10.1029/2003JB002756).
- Fialko, Y., D. Sandwell, and M. Simons (2005). Three-dimensional deformation caused by the Bam, Iran, earthquake and the origin of shallow slip deficit, *Nature* **435**, no. 7040, 295–299, doi: [10.1038/nature03425](https://doi.org/10.1038/nature03425).
- Fielding, E. J., Z. Liu, O. L. Stephenson, M. Zhong, C. Liang, A. Moore, S.-H. Yun, and M. Simon (2020). Surface deformation related to the 2019 M_w 7.1 and 6.4 Ridgecrest earthquakes in California from GPS, SAR interferometry, and SAR pixel offsets, *Seismol. Res. Lett.* doi: [10.1785/0220190302](https://doi.org/10.1785/0220190302).
- Floyd, M., G. Funning, Y. Fialko, R. Terry, and T. Herring (2020). Survey and Continuous GNSS in the Vicinity of the July 2019 Ridgecrest earthquakes, *Seismol. Res. Lett.* doi: [10.1785/0220190324](https://doi.org/10.1785/0220190324).
- Floyd, M. A., R. J. Walters, J. R. Elliott, G. J. Funning, J. L. Svarc, J. R. Murray, A. J. Hooper, Y. Larsen, P. Marinkovic, R. Bürgmann, *et al.* (2016). Spatial variations in fault friction related to lithology from rupture and afterslip of the 2014 South Napa, California, earthquake, *Geophys. Res. Lett.* **43**, 6808–6816, doi: [10.1002/2016GL069428](https://doi.org/10.1002/2016GL069428).
- Freed, A. M. (2005). Earthquake triggering by static, dynamic, and postseismic stress transfer, *Annu. Rev. Earth Planet. Sci.* **33**, 335–368, doi: [10.1146/annurev.earth.33.092203.122505](https://doi.org/10.1146/annurev.earth.33.092203.122505).
- Freed, A. M., S. T. Ali, and R. Bürgmann (2007). Evolution of stress in southern California for the past 200 years from coseismic, postseismic and interseismic stress changes, *Geophys. J. Int.* **169**, no. 3, 1164–1179, doi: [10.1111/j.1365-246X.2007.03391.x](https://doi.org/10.1111/j.1365-246X.2007.03391.x).
- Goldberg, D. E., D. Melgar, V. J. Sahakian, A. M. Thomas, X. Xu, B. W. Crowell, and J. Geng (2020). Complex rupture of an immature fault zone: A simultaneous kinematic model of the 2019 Ridgecrest, CA earthquakes, *Geophys. Res. Lett.* **47**, no. 3, e2019GL086382, doi: [10.1029/2019gl086382](https://doi.org/10.1029/2019gl086382).
- Haddon, E. K., C. B. Amos, O. Zielke, A. S. Jayko, and R. Burgmann (2016). Surface slip during large Owens Valley earthquakes, *Geochem. Geophys. Geosys.* **17**, no. 6, 2239–2269, doi: [10.1002/2015GC006033](https://doi.org/10.1002/2015GC006033).
- Hartzell, S. H., and T. H. Heaton (1983). Inversion of strong ground motion and teleseismic waveform data for the fault rupture history of the 1979 Imperial Valley, California, earthquake, *Bull. Seismol. Soc. Am.* **73**, 1553–1583.
- Hauksson, E., and J. Unruh (2007). Regional tectonics of the Coso geothermal area along the intracontinental plate boundary in central eastern California: Three-dimensional V_p and V_p/V_s models, spatial-temporal seismicity patterns, and seismogenic deformation, *J. Geophys. Res.* **112**, no. B004721, 1–24, doi: [10.1029/2006JB004721](https://doi.org/10.1029/2006JB004721).
- Hauksson, E., W. Yang, and P. M. Shearer (2012). Waveform relocated earthquake catalog for southern California (1981 to June 2011), *Bull. Seismol. Soc. Am.* **102**, no. 5, 2239–2244, doi: [10.1785/0120120010](https://doi.org/10.1785/0120120010).
- Hauksson, E., K. Hutton, H. Kanamori, L. Jones, J. Mori, S. Hough, and G. Roquemore (1995). Preliminary report on the 1995 Ridgecrest earthquake sequence in eastern California, *Seismol. Res. Lett.* **66**, no. 6, 54–60, doi: [10.1785/gssrl.66.6.54](https://doi.org/10.1785/gssrl.66.6.54).
- Hauksson, E., C. Yoon, E. Yu, J. R. Andrews, M. Alvarez, R. Bhadha, and V. Thomas (2020). Caltech/USGS Southern California Seismic Network (SCSN) and Southern California Earthquake Data Center (SCEDC): Data availability for the 2019 Ridgecrest sequence, *Seismol. Res. Lett.* doi: [10.1785/0220190290](https://doi.org/10.1785/0220190290).
- Hearn, E. H., and R. Bürgmann (2005). The effect of elastic layering on inversions of GPS data for coseismic slip and resulting stress changes: Strike-slip earthquakes, *Bull. Seismol. Soc. Am.* **95**, no. 5, 1637–1653, doi: [10.1785/0120040158](https://doi.org/10.1785/0120040158).
- Heaton, T. M (1990). Evidence for a and implications of self-healing pulses of slip in earthquake rupture, *Phys. Earth Planet. In.* **64**, 1–20.
- Herrmann, R. B. (2013). Computer programs in seismology: An evolving tool for instruction and research, *Seismol. Res. Lett.* **84**, no. 6, 1081–1088.
- Hough, S., and K. Hutton (2008). Revisiting the 1872 Owens Valley, California, earthquake revisiting the 1872 Owens Valley, California, earthquake, *Bull. Seismol. Soc. Am.* **98**, no. 2, 931–949, doi: [10.1785/0120070186](https://doi.org/10.1785/0120070186).
- Huang, H., R. Bürgmann, L. Meng, K. Wang, and B. Rousset (2019). Spatio-temporal foreshock evolution of the 2019 M 6.4 and M 7.1 Ridgecrest, California Earthquakes, *Poster Presentation at 2019 SCEC Annual Meeting*, Palm Springs, California, September 2019, SCEC Contribution 9723.
- Huang, M.-H., E. J. Fielding, H. Dickinson, J. Sun, J. A. G. Ortega, A. M. Freed, and R. Bürgmann (2017). Fault geometry inversion and slip distribution of the 2010 M_w 7.2 El Mayor-Cucapah earthquake from geodetic data, *J. Geophys. Res.* **122**, no. 1, 607–621, doi: [10.1002/2016JB012858](https://doi.org/10.1002/2016JB012858).

- Hudnut, K. W., B. A. Brooks, K. Scharer, J. L. Hernandez, T. E. Dawson, M. E. Oskin, J. Ramon Arrowsmith, C. A. Goulet, K. Blake, M. L. Boggs, *et al.* (2020). Airborne lidar and electro-optical imagery along surface ruptures of the 2019 Ridgecrest earthquake sequence, Southern California, *Seismol. Res. Lett.* doi: [10.1785/0220190338](https://doi.org/10.1785/0220190338).
- Jin, Z., and Y. Fialko (2020). Finite slip models of the 2019 Ridgecrest earthquake sequence constrained by space geodetic data and after-shock locations, *Bull. Seismol. Soc. Am.* doi: [10.1785/0120200060](https://doi.org/10.1785/0120200060).
- Johanson, I. A., and R. Bürgmann (2010). Coseismic and postseismic slip from the 2003 San Simeon earthquake and their effects on backthrust slip and the 2004 Parkfield earthquake, *J. Geophys. Res.* **115**, no. B006599, 1–18, doi: [10.1029/2009JB006599](https://doi.org/10.1029/2009JB006599).
- Johanson, I. A., E. J. Fielding, F. Rolandone, and R. Bürgmann (2006). Coseismic and postseismic slip of the 2004 Parkfield earthquake from space-geodetic data, *Bull. Seismol. Soc. Am.* **96**, S269–S282, doi: [10.1785/0120050818](https://doi.org/10.1785/0120050818).
- Johnson, C. W., Y. Fu, and R. Bürgmann (2017). Seasonal water storage, stress modulation, and California seismicity, *Science* **356**, 6343, 1161–1164, doi: [10.1126/science.aak9547](https://doi.org/10.1126/science.aak9547).
- Kaneko, Y., and Y. Fialko (2011). Shallow slip deficit due to large strike-slip earthquakes in dynamic rupture simulations with elasto-plastic off-fault response, *Geophys. J. Int.* **186**, no. 3, 1389–1403, doi: [10.1111/j.1365-246X.2011.05117.x](https://doi.org/10.1111/j.1365-246X.2011.05117.x).
- Kaverina, A., D. Dreger, and E. Price (2002). The combined inversion of seismic and geodetic data for the source process of the 16 October 1999 M_w 7.1 Hector Mine, California, earthquake, *Bull. Seismol. Soc. Am.* **92**, no. 4, 1266–1280.
- King, G., R. S. Stein, and J. Lin (1994). Static stress changes and the triggering of earthquakes, *Bull. Seismol. Soc. Am.* **84**, no. 3, 935–953, doi: [10.1016/0040-1951\(70\)90014-4](https://doi.org/10.1016/0040-1951(70)90014-4).
- Lauer, B., R. Grandin, and Y. Klinger (2020). Fault geometry and slip distribution of the 2013 M_w 7.7 Balochistan earthquake from non-linear and linear inversions of SAR and optical data, *J. Geophys. Res.* doi: [10.1029/2019JB018380](https://doi.org/10.1029/2019JB018380).
- Lee, J., J. Spencer, and L. Owen (2001). Holocene slip rates along the Owens Valley fault, California: Implications for the recent evolution of the eastern California shear zone, *Geology* **29**, no. 9, 819–822.
- Li, Y., R. Bürgmann, and B. Zhao (2020). Evidence of fault immaturity from shallow slip deficit and lack of postseismic deformation of the 2017 M_w 6.5 Jiuzhaigou earthquake, *Bull. Seismol. Soc. Am.* **110**, doi: [10.1785/0120190162](https://doi.org/10.1785/0120190162).
- Lin, G. (2020). Waveform cross-correlation relocation and focal mechanisms for the 2019 Ridgecrest earthquake sequence, *Seismol. Res. Lett.* doi: [10.1785/0220190277](https://doi.org/10.1785/0220190277).
- Liu, C., T. Lay, E. E. Brodsky, K. Dascher-Cousineau, and X. Xiong (2019). Coseismic rupture process of the large 2019 Ridgecrest earthquakes from joint inversion of geodetic and seismological observations, *Geophys. Res. Lett.* **46**, no. 21, 11820–11829.
- Liu, S., Z.-K. Shen, and R. Bürgmann (2015). Recovery of secular deformation field of Mojave shear zone in southern California from historical terrestrial and GPS measurements, *J. Geophys. Res.* **120**, no. 5, 3965–3990, doi: [10.1002/2015JB011941](https://doi.org/10.1002/2015JB011941).
- Lomax, A. (2020). Absolute location of 2019 Ridgecrest seismicity reveals a shallow M_w 7.1 hypocenter, migrating and pulsing M_w 7.1 foreshocks, and duplex M_w 6.4 ruptures, *Bull. Seismol. Soc. Am.* doi: [10.1785/0120200006](https://doi.org/10.1785/0120200006).
- Magen, Y., A. Ziv, A. Inbal, G. Baer, and J. Hollingsworth (2020). The Ridgecrest conjugate earthquake pair: A joint slip inversion of InSAR, optical imagery and GPS, *Bull. Seismol. Soc. Am.* doi: [10.1785/0120200024](https://doi.org/10.1785/0120200024).
- Mattioli, G. S., D. A. Phillips, K. M. Hodgkinson, C. Walls, D. J. Mencin, B. A. Bartel, D. J. Charlevoix, C. Crosby, M. J. Gottlieb, B. Henderson, *et al.* (2020). The GAGE data and field response to the 2019 Ridgecrest earthquake sequence, *Seismol. Res. Lett.* doi: [10.1785/0220190283](https://doi.org/10.1785/0220190283).
- McClusky, S. C., S. C. Bjornstad, B. H. Hager, R. W. King, B. J. Meade, M. M. Miller, F. C. Monastero, and B. J. Souter (2001). Present-day kinematics of the eastern California shear zone from a geodetically constrained block model, *Geophys. Res. Lett.* **28**, no. 17, 3369–3372, doi: [10.1029/2001GL013091](https://doi.org/10.1029/2001GL013091).
- Miller, M. M., D. J. Johnson, T. H. Dixon, and R. K. Dokka (2001). Refined kinematics of the eastern California shear zone from GPS observations, 1993–1998, *J. Geophys. Res.* **106**, no. B2, 2245–2263, doi: [10.1029/2000JB900328](https://doi.org/10.1029/2000JB900328).
- Milliner, C., and A. Donnellan (2020). Using daily observations from planet labs satellite imagery to separate the surface deformation between the 4 July M_w 6.4 Foreshock and 5 July M_w 7.1 Mainshock during the 2019 Ridgecrest earthquake sequence, *Seismol. Res. Lett.* doi: [10.1785/0220190271](https://doi.org/10.1785/0220190271).
- Milliner, C. W. D., J. F. Dolan, J. Hollingsworth, S. Leprince, F. Ayoub, and C. G. Sammis (2015). Quantifying near-field and off-fault deformation patterns of the 1992 M_w 7.3 Landers earthquake, *Geochem. Geophys. Geosys.* **16**, 1577–1598, doi: [10.1002/2014GC005693](https://doi.org/10.1002/2014GC005693).
- Nalbant, S., A. Hubert, and G. C. P. King (1998). Stress coupling between earthquakes in northwest Turkey and the north Aegean Sea, *J. Geophys. Res.* **103**, 24,469–24,486.
- Nicholson, C., A. Plesch, and J. H. Shaw (2017). Community fault model version 5.2: Updating & expanding the CFM 3D fault set and its associated fault database, *Poster Presentation at 2017 SCEC Annual Meeting*, September 2017, SCEC Contribution 7735.
- Oglesby, D. D., and P. M. Mai (2012). Fault geometry, rupture dynamics and ground motion from potential earthquakes on the North Anatolian fault under the Sea of Marmara, *Geophys. J. Int.* **118**, no. 3, 1071–1087, doi: [10.1111/j.1365-246X.2011.05289.x](https://doi.org/10.1111/j.1365-246X.2011.05289.x).
- Ohnaka, M., and T. Yamashita (1989). A cohesive zone model for dynamic shear faulting based on experimentally inferred constitutive relation and strong motion source parameters, *J. Geophys. Res.* **94**, 4089–4104.
- Okada, Y. (1985). Surface deformation due to shear and tensile faults in a half-space, *Bull. Seismol. Soc. Am.* **75**, no. 4, 1135–1154.
- Parsons, T. (2000). Heightened odds of large earthquakes near Istanbul: An interaction-based probability calculation, *Science* **288**, no. 5466, 661–665, doi: [10.1126/science.288.5466.661](https://doi.org/10.1126/science.288.5466.661).
- Parsons, T. E., and D. S. Dreger (2000). Static-stress impact of the 1992 Landers earthquake sequence on nucleation and slip at the site of the 1999 M 7.1 Hector Mine earthquake, southern California, *Geophys. Res. Lett.* **27**, no. 13, 1949–1952.
- Peltzer, G., F. Crampé, S. Hensley, and P. Rosen (2001). Transient strain accumulation and fault interaction in the eastern California shear zone, *Geology* **29**, no. 11, 975–978.
- Perfettini, H., R. S. Stein, R. W. Simpson, and M. Cocco (1999). Stress transfer by the 1988–1989 M 5.3 and 5.4 Lake Elsmar foreshocks

- to the Loma Prieta fault; unclamping at the site of peak mainshock slip, *J. Geophys. Res.* **104**, no. B9, 20,169–20,182.
- Perrin, C., I. Manighetti, J. P. Ampuero, F. Cappa, and Y. Gaudemer (2016). Location of largest earthquake slip and fast rupture controlled by along-strike change in fault structural maturity due to fault growth, *J. Geophys. Res.* **121**, no. 5, 3666–3685.
- Plesch, A., J. H. Shaw, C. Benson, W. A. Bryant, S. Carena, M. Cooke, J. Dolan, G. Fuis, E. Gath, L. Grant, *et al.* (2007). Community fault model (CFM) for southern California, *Bull. Seismol. Soc. Am.* **97**, no. 6, 1793–1802, doi: [10.1785/0120050211](https://doi.org/10.1785/0120050211).
- Pollitz, F., J. R. Murray, S. E. Minson, E. Phillips, J. L. Svarc, C. W. Wicks, M. H. Murray, T. L. Ericksen, B. A. Brooks, E. A. Roeloffs, *et al.* (2019). Observations and models of crustal deformation transients following the 2019 Ridgecrest, California, earthquake sequence, *AGU Fall Meeting Abstract*, December 2019.
- Ponti, D. J., J. Luke Blair, C. M. Rosa, K. Thomas, A. J. Pickering, S. Akciz, S. Angster, J.-P. Avouac, J. Bachhuber, S. Bacon, *et al.* (2020). Documentation of surface fault rupture and ground deformation features produced by the Ridgecrest M 6.4 and M 7.1 earthquake sequence of 4 July and 5, 2019, *Seismol. Res. Lett.* doi: [10.1785/0220190322](https://doi.org/10.1785/0220190322).
- Rice, R. R., C. G. Sammis, and R. Parsons (2005). Off-fault secondary failure induced by a dynamic slip-pulse, *Bull. Seismol. Soc. Am.* **95**, 109–134.
- Ross, Z. E., B. Idini, Z. Jia, O. L. Stephenson, M. Zhang, X. Wang, Z. Zhan, M. Simons, E. Fielding, S. Yun, *et al.* (2019). Hierarchical interlocked orthogonal faulting in the 2019 Ridgecrest earthquake sequence, *Science* **366**, no. 6463, 346–351, doi: [10.1126/science.aaz0109](https://doi.org/10.1126/science.aaz0109).
- Scholz, C. H. (1998). Earthquakes and friction laws, *Nature* **391**, no. 6662, 37–42.
- Shelly, D. R. (2020). A high-resolution seismic catalog for the initial 2019 Ridgecrest earthquake sequence: Foreshocks, aftershocks, and faulting complexity, *Seismol. Res. Lett.* 1–8, doi: [10.1785/0220190309](https://doi.org/10.1785/0220190309).
- Shen, Z.-K., D. D. Jackson, and Y. Y. Kagan (2007). Implications of geodetic strain rate for future earthquakes, with a five-year forecast of M 5 earthquakes in southern California, *Seismol. Res. Lett.* **78**, no. 1, 116–120, doi: [10.1785/gssrl.78.1.116](https://doi.org/10.1785/gssrl.78.1.116).
- Simons, M. (2002). Coseismic deformation from the 1999 M_w 7.1 Hector Mine, California, earthquake as inferred from InSAR and GPS observations, *Bull. Seismol. Soc. Am.* **92**, no. 4, 1390–1402, doi: [10.1785/0120000933](https://doi.org/10.1785/0120000933).
- Smith, D. E., and T. H. Heaton (2011). Models of stochastic, spatially varying stress in the crust compatible with focal-mechanism data, and how stress inversions can be biased toward the stress rate, *Bull. Seismol. Soc. Am.* **101**, 1396–1421, doi: [10.1785/0120100058](https://doi.org/10.1785/0120100058).
- Somerville, P., K. Irikura, S. Sawada, D. J. Wald, N. Abrahamson, Y. Iwasaki, T. Kagawa, N. Smith, and A. Kowada (1999). Characterizing crustal earthquake slip models for the prediction of strong ground motion, *Seismol. Res. Lett.* **70**, no. 1, 59–80.
- Southern California Earthquake Data Center (SCEDC) (2013). Southern California Earthquake Data Center, Caltech. Dataset, doi: [10.7909/C3WD3xH1](https://doi.org/10.7909/C3WD3xH1).
- Toda, S., R. Stein, K. Richards-Dinger, and S. Bozkurt (2005). Forecasting the evolution of seismicity in southern California: Animations built on earthquake stress transfer, *J. Geophys. Res.* **110**, no. B5, 97, doi: [10.1029/2004JB003415](https://doi.org/10.1029/2004JB003415).
- Surpless, B. (2008). Modern strain localization in the central Walker Lane, western United States: Implications for the evolution of intraplate deformation in transtensional settings, *Tectonophysics* **457**, nos. 3/4, 239–253, doi: [10.1016/j.tecto.2008.07.001](https://doi.org/10.1016/j.tecto.2008.07.001).
- Unruh, J., and J. Humphrey (2017). Seismogenic deformation between the Sierran microplate and Oregon Coast block, California, USA, *Geology* **45**, no. 5, 415–418, doi: [10.1130/g38696.1](https://doi.org/10.1130/g38696.1).
- Wang, K., and R. Bürgmann (2020). Co- and early postseismic deformation due to the 2019 Ridgecrest earthquake sequence constrained by Sentinel-1 and COSMO–SkyMed SAR data, *Seismol. Res. Lett.* doi: [10.1785/0220190299](https://doi.org/10.1785/0220190299).
- Wang, K., and Y. Fialko (2018). Observations and modeling of coseismic and postseismic deformation due to the 2015 M_w 7.8 Gorkha (Nepal) Earthquake, *J. Geophys. Res.* **123**, no. 1, 761–779, doi: [10.1002/2017JB014620](https://doi.org/10.1002/2017JB014620).
- Wang, R., F. Martin, and F. Roth (2003). Computation of deformation induced by earthquakes in multi-layered elastic crust: FORTRAN programs EDGRN/EDCMP, *Comput. Geosci.* **29**, 195–207, doi: [10.1016/S0098-3004\(02\)00111-5](https://doi.org/10.1016/S0098-3004(02)00111-5).
- Wollherr, S., A. A. Gabriel, and P. M. Mai (2019). Landers 1992 “reloaded”: Integrative dynamic earthquake rupture modeling, *J. Geophys. Res.* **124**, 6666–6702, doi: [10.1029/2018JB016355](https://doi.org/10.1029/2018JB016355).
- Xu, X., D. T. Sandwell, and B. Smith-Konter (2020). Coseismic displacements and surface fractures from Sentinel-1 InSAR: 2019 Ridgecrest earthquakes, *Seismol. Res. Lett.* doi: [10.1785/0220190275](https://doi.org/10.1785/0220190275).
- Xu, X., X. Tong, D. T. Sandwell, C. W. D. Milliner, J. F. Dolan, J. Hollingsworth, S. Leprince, and F. Ayoub (2016). Refining the shallow slip deficit, *Geophys. J. Int.* **204**, no. 3, 1843–1862, doi: [10.1093/gji/ggv563](https://doi.org/10.1093/gji/ggv563).
- Yue, H., J. Sun, M. Wang, Z. Shen, Y. Zhou, W. Lu, and L. Xue (2019). Seismic and aseismic slips contributed to the foreshock-to-mainshock triggering during the July 2019 Ridgecrest earthquake sequence, *AGU 2019 Fall Meeting*, San Francisco, California, December 2019, S31G-0508.

Manuscript received 4 March 2020